4

Techniques and Applications of Scanning Acoustic Microscopy in Bone Remodeling Studies

Mark C. Zimmerman
New Jersey Medical School

Robert D. Harten, Jr.
New Jersey Medical School

Sheu-Jane Shieh
Wayne State University

Alain Meunier
L' Hopital St. Louis

J. Lawrence Katz
Case Western Reserve University

4.1 Acoustic Microscopy Theory, Techniques, and Specimen Preparation

The Physical Interaction between Ultrasound and Solid Media

Acoustic microscopy is akin to optical microscopy — both are techniques that create magnified images of objects. However, where optical microscopy uses waves of light to form its image, acoustic microscopy uses waves of high frequency sound, or ultrasound. The examination of an object with ultrasound creates an image of the object's material and mechanical properties, rather than an image of optical features. The physical interaction of ultrasound with matter is the basis of all acoustic microscopy images.

Presently, almost all acoustic microscopy uses the principle of reflection. When a sound wave is directed onto a large interface, it will be partially transmitted across the interface and partially reflected back toward its source. The reflected portion of the wave is used to determine the mechanical properties of the materials of the interface. The percentage of the wave reflected at the interface depends on the wave's angle of incidence and the acoustic impedance differences of the materials that make up the interface. Snell's law states that for a wave undergoing specular reflection, the angle of incidence equals the angle of reflection. In an acoustic microscope, the source of sound is a piezoelectric transducer which acts as a sender and receiver. Therefore, for the transducer to receive the maximum reflected signal, the transducer is oriented so that the incident wave strikes the interface perpendicularly. The path of the reflected wave thus will also be perpendicular to the interface.

Acoustic impedance is the product of the density and the velocity of ultrasound in the material. The symbol for acoustic impedance is Z and the units are Rayleighs, abbreviated as Rayls. Acoustic impedances are most often reported in MRayls, where 1 MRayl = 10^6 kg m^{-2} s^{-1}. The velocity of ultrasound in biological tissues varies negligibly over a wide range of frequencies; that is, it is nondispersive. The acoustic impedance of a tissue is constant with changing frequency. For reflection at an interface, the pressure of the reflected wave is determined by the difference in acoustic impedance between the two media at the interface. The larger the difference in acoustic impedance at the interface, the greater the pressure of the wave reflected back toward the transducer. Conversely, if the acoustic impedance of the media on each side of the interface is the same, all of the incident beam is transmitted and none will be reflected.

For optimum imaging in acoustic microscopy, the sound pressure after reflection must be maximized, and for this a liquid-solid interface is used. That is, to examine a solid like bone, a liquid couplant is used to propagate sound from the transducer to the bone specimen. To illustrate this, consider sound traveling through water, which has an acoustic impedance of 1.5 MRayls at 20°C, becoming incident on bone, which has an acoustic impedance of approximately 7.8 MRayls. The coefficient of reflection, R, is computed by the formula:

$$R = \frac{Z_2 - Z_1}{Z_2 + Z_1}$$

where Z_1 and Z_2 are the acoustic impedances of the two interfacial media, water and bone. Expressed as a percentage, the reflected wave will have 68% of the sound pressure of the incident wave. However, this large amplitude is not the amplitude of the wave received by the transducer. As the reflected wave travels through the water on the return path toward the transducer, it is attenuated and suffers a loss in intensity. Moreover, this attenuation increases with increasing frequency. This is a practical limitation of reflection acoustic microscopy which prevents it from being used to study softer materials such as soft biological tissues which have acoustic impedances only slightly higher than water.

Attenuation in the second media at the interface is not a concern in this case. Although the transmitted wave traveling through the second media will undergo attenuation, the reflected wave will not be affected. It is evident upon inspection of the reflection coefficient formula that the acoustic impedance of the second material at an interface may be determined if the acoustic impedance of the first material is known and the reflection coefficient measured.

The Relationship between Acoustic Impedance and Mechanical Properties

Once the acoustic impedance of a material is determined, the relation to the mechanical properties of a material may be assessed. As stated earlier, acoustic impedance is a function of material density and velocity. It will now be shown that the mechanical properties of stiffness, in particular, the bulk modulus, Young's modulus, and the shear modulus are also functions of the same material density and velocity.

When the wave equation which describes the displacement of a harmonic wave is substituted into the general equation of motion of a continuum, a relation is established between the velocity of propagation and stress since, in the equation of motion, the force exerted on a solid is the gradient of the stress. (For

a full derivation, the reader is referred to Beyer and Lechter and Kolsky.[1,2]) If Hooke's law for a linear elastic solid is also substituted into this equation, the equation:[*]

$$C_i = \sqrt{k + \tfrac{4}{3}\,G/\rho}$$

results for isotropic, homogeneous media. This is the equation for the bulk longitudinal dilatational velocity C, in an infinitely extended medium of bulk modulus k, shear modulus G, and density ρ. In a bar subject to a longitudinal wave, if the wavelength is long compared to the lateral dimensions, the entire cross section is subject to uniform stress and displacement and the velocity of propagation extensional longitudinal is the bar wave velocity C, where:[**]

$$C_L = \sqrt{E/\rho}$$

and E is Young's modulus. The distinction in the two velocity equations exists because of the difference in the relative dimensions of the wavelength and the media. In the first case, the propagation of longitudinal waves subjects the infinitely extended media to compression and shear, and thus the shear modulus and the bulk modulus are involved.

These two velocity equations and the equation of acoustic impedance show that the material moduli and the acoustic parameter Z are dependent on the same physical constants, namely, density and velocity. Therefore, a direct proportionality exists between the acoustic impedance and the mechanical properties of a material. With acoustic microscopy, a measure of the mechanical properties of a material may be determined by invoking their proportionality with acoustic impedance. Moreover, acoustic microscopy affords a great advantage over traditional mechanical testing — the ability to determine mechanical properties on a submillimeter level. This ability is derived from the use of ultrasound that can be focused to spot sizes smaller than one millimeter.

The Spatial Resolution of the Acoustic Microscope

The fundamental components of the acoustic microscope are the transducer and lens. A single flat element piezoelectric transducer acts as sender and receiver, generating and acquiring pulses of waves. By refraction, a spherical lens focuses the plane waves that are excited by the transducer. The intensity of the ultrasound beam reaches its peak at a distance from the lens equal to its focal length. In the focal region, the beam narrows, and the energy is concentrated into a smaller area. The size of this area is the spatial resolution of the beam. The transducer is positioned above the media to be interrogated at the focal length to achieve maximum reflection of the incident wave.

Transducers used in acoustic microscopy differ mainly in their frequency, focal length, size, and the ratio of the focal length to aperture (known as the F number). A transducer with a focal length of 32 mm and diameter of 16 mm has an F number of F2. The acceptance angle of a transducer is the maximum angle relative to its long axis at which acoustic waves are sent or received. The sine of the acceptance angle θ_{max} is one-half the radius of curvature divided by the diameter or

$$\sin\theta_{max} = \frac{1}{2}F$$

Particular transducers are designed with an acceptance angle below the critical cutoff angle for which Rayleigh rays are generated to ensure that only specular reflection exists.

The spatial resolution of a transducer depends on the operating frequency, coupling medium, and transducer properties. The relation between resolution and frequency is demonstrated in the equation:

---

[*]Uniaxial with lateral constraints.

[**]Equivalent to uniaxial mechanical test.

$$\lambda = c/f$$

where λ is wavelength, c is velocity, and f is frequency. The smaller the wavelength (the higher the frequency), the finer the spatial resolution will be. This equation assumes that the ultrasonic wave is comprised of a single frequency.

In reality it is impossible for a pulsed transducer to generate a single frequency signal because of inertial effects. The bandwidth of a signal is the range of frequencies in the ultrasound pulse — shorter pulses will have larger bandwidths. In acoustic microscopy, short pulses are necessary to ensure that incident and reflected waves do not interfere. A transducer that has short pulse lengths has a short "ring down time" because it oscillates through fewer numbers of cycles per excitation.

A Historical Perspective of the Study of Bone with Acoustic Microscopy

The first practical scanning acoustic microscope was developed and built for materials analysis by Lemons and Quate.[3] Jipson and Quate[4] improved the acoustic microscope, enabling it to obtain resolutions comparable to those of an optical microscope. Since then, scanning acoustic microscopy has become a major nondestructive evaluation tool involving imaging and the characterization and detection of defects in structural materials.[5,6] As the acoustic waves travel through the specimen, it can be focused at different levels within the sample, permitting the technique to produce images which feature the surface or the subsurface of a specimen.

Although acoustic microscopy has been used for over 3 decades in industry to analyze solid materials, only recently have scientists applied scanning acoustic microscopy to the fields of biology and medicine, where "soft" materials are prevalent. Experiments involving the technique have been used to study the acoustic velocity, acoustic attenuation, density, and thickness of tissues, and even cells.[7-12] Because of their structures and calcified natures, bones and teeth have higher acoustic reflectivities than soft tissue, and to date most studies have used acoustic microscopy for the qualitative examination of bone.[10,11,13-17]

Some very interesting high resolution qualitative observations have been made by Katz and Meunier.[18] Their findings will be discussed in more detail in Section 4.2.

To measure the acoustic impedance of a material, one collects the amplitude of the first echo of a longitudinal sound wave reflected from the surface of the specimen. Meunier et al.[14] have verified this technique with bone as well as many other materials. By varying transducer design, other sonic waves can be generated and used for material properties analysis. Gardner et al.[19] have demonstrated that with a technique of defocusing Rayleigh waves, the material properties of many materials can be measured. Rayleigh waves are surface waves; however, bone poorly supports Rayleigh wave propagation. High signal attenuation occurs because of the porosity of bone. Low Rayleigh velocities result, and given the angle at which the signal returns to the transducer, it is not possible for the transducer to receive the signal. The same group measured surface skimming waves from horse radial bone. A high frequency point focus lens was used and surface waves were measured every 150 microns in a line. The averaged velocities were used to calculate a mean elastic coefficient.

Other investigators have also used the velocities measured with acoustic microscopy to calculate the material properties of bone. Hasegawa et al.[20] used an acoustic microscope to measure the velocity of biopsied human bone specimens. They observed a significant decrease in the velocity of sound in osteoporotic bone compared to age-matched normal bone. Three other recently published studies have addressed the material property contributions that mineral and collagen provide for bone, and all three research groups utilized a scanning acoustic microscope. Broz et al.[21] used a number of material analysis techniques (including acoustic microscopy) to analyze the material properties of serially demineralized bone. All the techniques demonstrated decreased material properties with demineralization. Turner et al.[22] also used an acoustic microscope to study the collagen and mineral anisotropy of bone. They also compared the elastic constants generated with bulk transmission ultrasound against the constants generated with velocities measured with an acoustic microscope. Orthotropic symmetry was assumed, and

a good agreement with both techniques was observed, except for specimens oriented 30° to the longitudinal axis of the bone.

This deviation supports the hypothesis that the principal orientation of the secondary lamellar bone collagen is 30° to the long axis of the bone. This concept was further supported by the anisotropy ratio data generated in this study. The most recent work from Turner's laboratory[23] makes use of the collagen and mineral orientation data in a composite model for the ultrastructure of osteonal bone. A two-phase composite model was developed and the acoustic data played a key role in testing hypotheses regarding amounts of intrafibular vs. extrafibular mineral and collagen orientation.

A scanning acoustic microscope with a similar transducer was used in the studies by Hasegawa,[20] Turner,[22] Pidaparti,[23] and Broz.[21] Hasegawa, Turner, and Pidaparti reported a resolution of 60 microns and a precision of 0.3 to 0.5%. Broz et al. reported that their transducer produced a 100 μm resolution and scans were done with 50 micron stepping. In all four studies, acoustic velocity measurements were made at multiple locations on each specimen and then averaged for a mean velocity. Bulk density measurements were made using Archimedes' principle for the entire specimen and bulk elastic stiffness coefficients were calculated. These data were used to calculate the bulk elastic stiffness coefficients of the specimens. Thus, a relatively high resolution velocity measurement tool was used to measure multiple velocities, and a mean velocity was used to calculate bulk properties in all four studies.

Specimen Preparation

In all the experiments to be described, fresh or imbedded bone was tested. The imbedded bone goes through a dehydration and clearing process before imbedding in polymethylmethacrylate. After imbedding, the specimens are sectioned with a diamond saw and polished with fine sized grit until a 600 grit (approximately 15 μm) finish is attained. In all scanning experiments, deionized water was used as a couplant. An optical reflection microscope was used to examine the quality of the polishing and detect any defects or cracks that would affect the acoustic measurements. Once the specimen was aligned in the instrument, the parallelism assured that the wave front was always perpendicular to the specimen. Finally, each section was placed in an ultrasonic cleaner for 5 minutes to clear the bone of any grit that may have entered the pores during the polishing process.
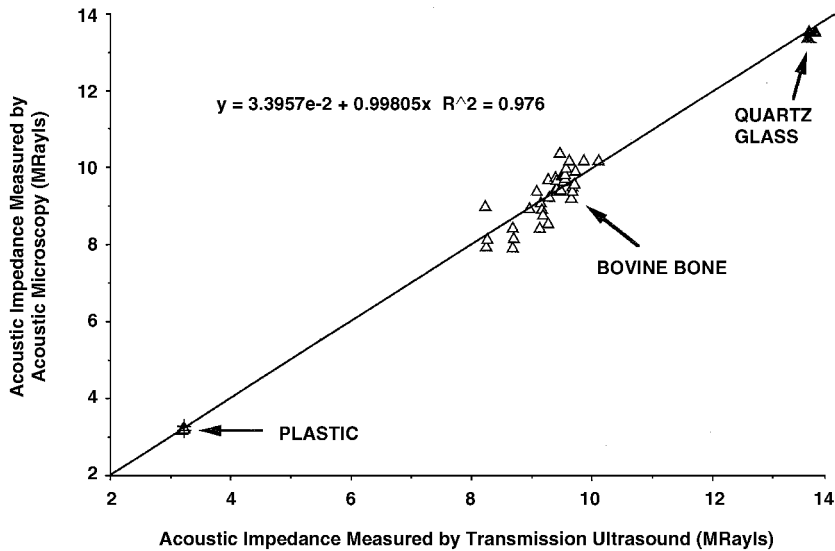
The Acoustic Microscope

The acoustic microscope used in the low frequency studies consisted of a Panametrics 5052UA ultrasonic analyzer, Matec SR-9000 pulser receiver, a differential amplifier, and a 12-bit A/D converter. The specimens were mounted in a water bath and scanned in a raster fashion with a 50 MHz spherically focused transducer (Panametrics Inc., V3204, 12.7 mm focal length). A microprocessor served multiple functions. It drove the scanning of the specimen, it acquired the data through an A/D converter (a 256×256 array of points per image is stored), and it presented the results visually.

The resolution of the images ranged from 20 to 140 microns depending on the stepping distance. The 50 MHz transducer used in these studies had a spot size of 20 microns, which dictated the maximum resolution of this system. Software developed for this application produces a pseudo-color map of the acoustic impedance of the surface of the specimen in two or three dimensions, where either color (2D) or profile (3D) is indicative of reflected acoustic impedance. The depth of penetration of the analyses varies from roughly 20 to 80 μm in well-mineralized bone. The depth of penetration is approximately equal to one wavelength which is equal to the speed of sound in water divided by the frequency of the transducer (1500m/s divided by 50MHz). Thus, in materials with higher acoustic velocities, e.g., more mature bone, the depth of penetration is greater.

This program also allows quantitative mapping of the coefficient of reflection, area, and thresholding with numerical data in an easily accessible data array. The acoustic impedance is determined from the acquired amplitude information through a calibration scheme using reference materials. Two homogeneous materials of known acoustic impedance are routinely scanned under the same operating conditions

as the experimental specimens. Typically, glass with an acoustic impedance of 13.56 MRayl and plastic (Plexiglas®) with an acoustic impedance of 3.23 MRayl are used. The impedances of the glass and plastic were previously determined in a separate transmission ultrasonic experiment, and verified by comparison with published data.[24]

A very simple experiment was conducted to evaluate the validity of our calibration scheme and the accuracy of our acoustic impedance measurements with our acoustic microscope.[25] This experiment entailed the sectioning and processing of bovine femoral bone. The bone was scanned, and the impedances measured using our calibration algorithm. A standard ultrasonic transmission technique[26] was used to also measure the acoustic impedance of the specimens. Using this technique, the impedance was simply the product of the transmission velocity and the density of the specimen. As shown in Fig. 4.1, an excellent correlation was observed between the two techniques ($r^2 = 0.976$). This verified that the system accurately measured impedance and the calibration scheme was adequate.

FIGURE 4.1 A graphical representation of acoustic impedance of bovine bone measured with a scanning acoustic microscope vs. a standard ultrasonic transmission technique. An excellent correlation was observed for the two techniques.

A secondary finding in this study was the effect of plastic imbedding on the acoustic properties of bone. The fresh bovine specimens scanned for the calibration experiment were then imbedded in polymethylmethacrylate (PMMA) as previously described, repolished, and scanned again. A small but statistically significant increase was observed for the imbedded specimens (0.4 MRayls). The increase was most likely caused by the filling of the pores of the bone with PMMA. This small increase can be eliminated by simply thresholding the window of acoustic properties to be analyzed. Thus, if the lower limit of a threshold window is set above the impedance of PMMA (3.18 Mrayls), then the effects of imbedding are eliminated.

The high frequency studies were performed using an Olympus UH3 SAM in the burst mode (a train of 10 or so sinusoids) at frequencies from 200 MHz (resolution 15 μm) to 1 GHz (resolution 1 μm). Unfortunately the depth of penetration is reduced considerably in well-mineralized bone at these frequencies compared to the 20 to 80 μm cited above; at 1 GHz it is down to a few μm. Therefore, the high frequency studies were mostly of the surface properties.

4.2. Acoustic Studies of Cortical Bone Material Properties

Low Frequency

The purpose of these experiments was to evaluate the acoustic properties of cortical bone. In the three studies to be described, specimens were taken from the femurs of humans or bovine species. The femur was chosen as the source of this tissue because of its biomechanical function, size, and the fact that its mechanical and material properties have been intensely investigated in previous studies. Additionally, of all the locations throughout the appendicular skeleton, cortical bone from the shaft of the femur is typically the most uniform and dense. Therefore, samples from this region are easier to fabricate, and the determination of averaged or bulk properties involves less experimental error due to the consistent nature of this tissue.

In the first study, six pairs of human femurs (3 males and 3 females, mean age of 85.6) were harvested and frozen. The central portion of each femur, 70% of the biomechanical length as defined by Bloebaum et al.,[27] was divided into ten 10 mm sections which were transversely cut beginning at the distal border of the lesser trochanter. Section 1 corresponded to the section closest to the hip and section 10 to the section closest to the knee. Fig. 4.2 shows the anatomic positions of the sections and the average impedance/section.
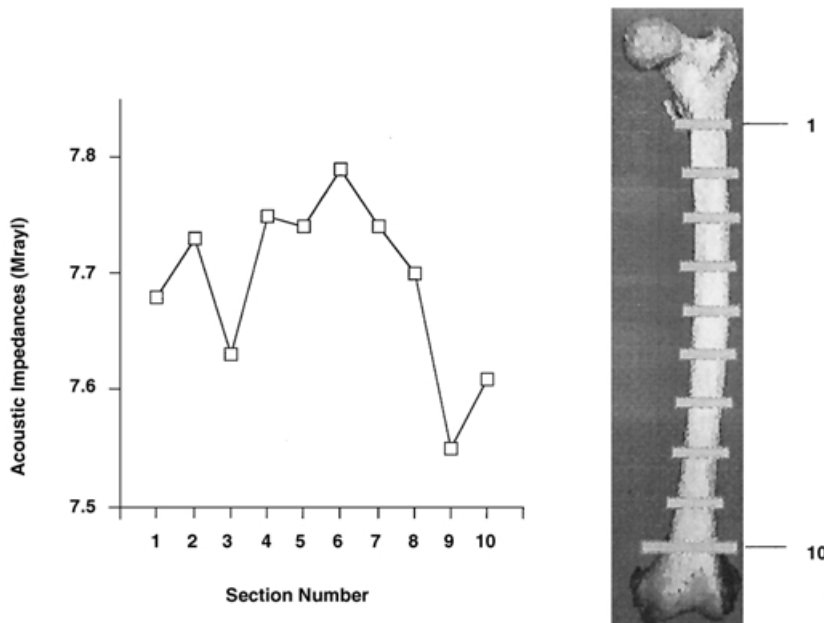

FIGURE 4.2   An image of the human femora and section locations for scanning acoustic microscopy.

Graphic images were stored as 256 × 256 arrays at a resolution of 140 microns. Acoustic impedance was measured for the entire cross section as well as for four quadrants within each cross section of bone. These four quadrants were designated with respect to anatomic position: anterior, posterior, medial, and lateral. High resolution scanning was also accomplished for a number of specimens consisting of a 1024 × 1024 array of data points with 20 micron resolution. These images were used primarily for a qualitative analysis of local properties.

Of the four factors analyzed (side, quadrant, sex, and cross-section number), only the cross-section number and the quadrant were significant factors affecting the impedance level ($p = 0.0018$ and $p = 0.0001$, respectively). Longitudinally, the acoustic properties of the cross sections peaked at mid-shaft. For instance, levels for sections 3, 9, and 10 were significantly lower than that for section 6. From a quadrant perspective, a Tukey's multiple comparison test showed the posterior quadrant to have a lower
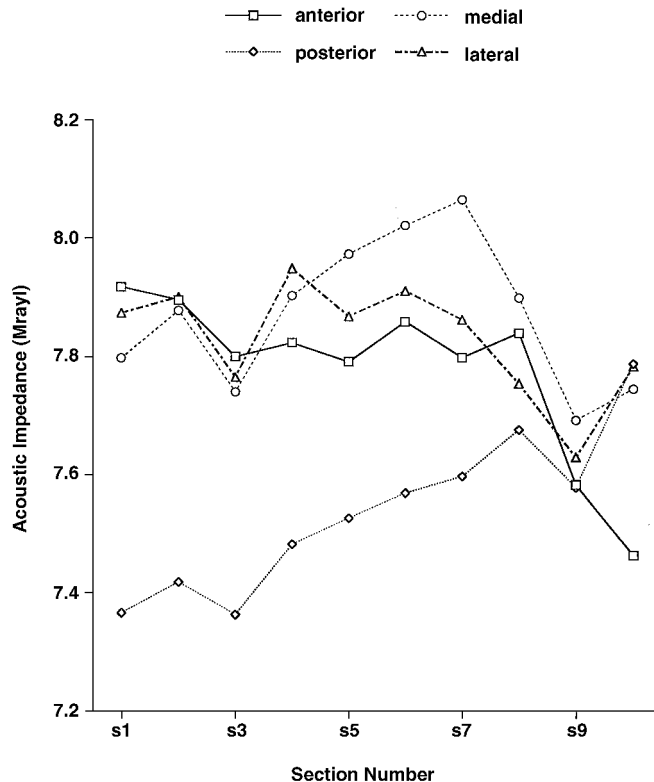
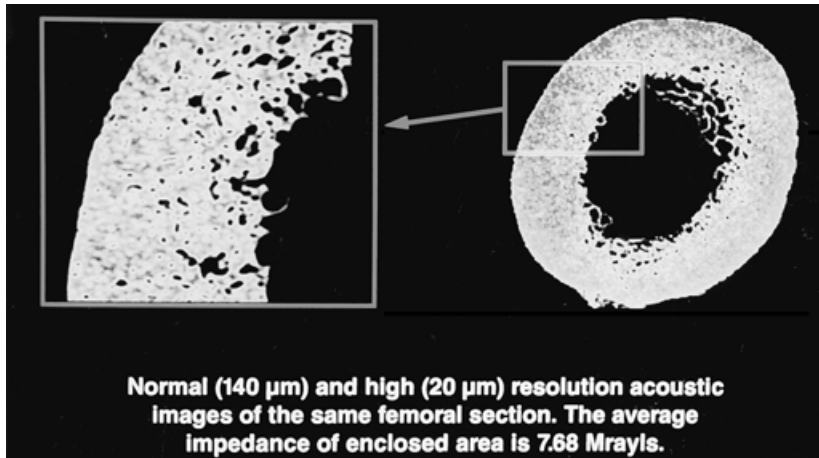**FIGURE 4.3** A graph highlighting the mean acoustic impedances within the human femoral cross sections.

impedance than the other quadrants (Fig. 4.3). Within the transverse sections, the posterior quadrant had statistically significantly lower impedances for the six most proximal sections. Proceeding distally, the impedance values of the four quadrants appear to converge on one another. It is interesting to note that the impedance of the anterior quadrant was significantly less than those of the three other quadrants in the most distal section.

The impedance variations observed at the different levels along the length of the femur, as well as within the cross sections, mirror the longitudinal elastic coefficient (C_{33}) and density variations obtained previously by Ashman et al.[26] and Meunier et al.[28] Ashman only analyzed the middle 40% of the femur, which corresponds to sections 3 through 7 in the present study. They observed that the density and elastic stiffness coefficient were greater at the 50, 60, and 70% levels of the femur relative to the 30 and 40% levels. In the present study, those parameters for levels 4, 5, 6, and 7 were greater than those for the other levels. Ashman also observed a statistically significant decrease in the elastic stiffness coefficient and the density of the posterior quadrant relative to the other quadrants.

Fig. 4.4 is an acoustic scan of a cross section taken from the left femur of an 86-year-old male. This example shows very uniform acoustic properties. The mean acoustic impedance of the most proximal segment (section 1) is 7.50 MRayls and the lateral zone shown by the box has an average impedance of 7.68 MRayls. Local variations in bone mineralization and structure result in local impedance differences which are shown by yellow and orange colors. The higher resolution scan of the local region has an approximate resolution of 20 microns.

Fig. 4.5 is an example of scans taken from bones with varying porotic and impedance properties. The left scan is a severely osteoporotic section taken from an 88-year-old female with an average impedance of 7.78 Mrayls. The image on the right is taken from the femur of an 86-year-old male, and has an average impedance of 7.98 MRayls. There is a striking difference in bone volume and color histograms show the

Normal (140 μm) and high (20 μm) resolution acoustic images of the same femoral section. The average impedance of enclosed area is 7.68 Mrayls.

FIGURE 4.4 A low and high resolution acoustic scan of an 86-year-old male. The two resolutions are highlighted and the histogram shows the variation in the acoustic properties.

88 year old female mean impedance = 7.78 Mrayls

86 year old male mean impedance = 7.98 Mrayls
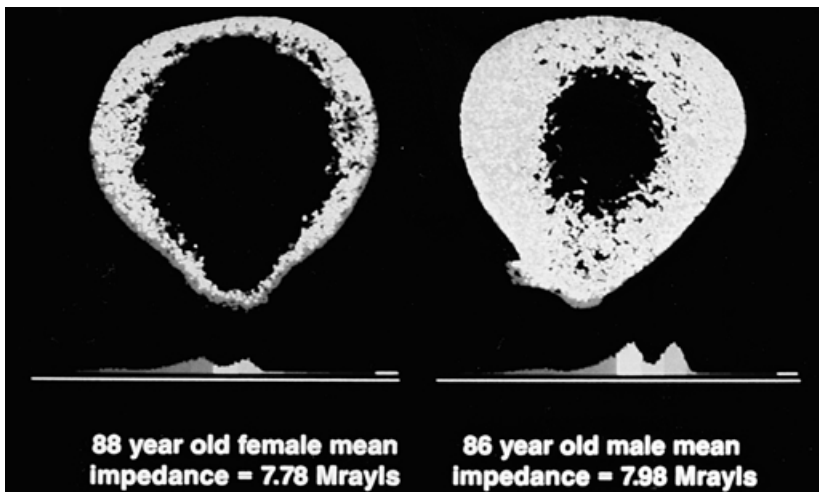
FIGURE 4.5 Two transverse cross sections taken from an 88-year-old female and an 86-year-old male at level 5. The female femur was severely osteoporotic while the male femur has good bone quality with an impedance histogram that shows greater volume and impedance.

volume of bone of varying properties. Both scans have bimodal distributions of acoustic properties, although a significant shift to the right, or a general increase, is apparent in the non-porotic bone from the male. Also of note is the lower impedance periosteal bone of the porotic femur, and the amount of lower impedance or "green" bone throughout the section. Additionally, islands of higher impedance bone are seen throughout the section with the antero-lateral section recording some of the highest values. This image demonstrates the highly dynamic nature of osteoporotic bone and the subsequent disproportionate property distribution that is a function of bone remodeling.

This was also observed by Meunier et al.[28] when bone sections that exhibited very low average acoustic characteristics still presented numerous locations with high acoustic properties. They observed that the decrease in the elastic properties due to bone remodeling is not a uniform process throughout the cortex

but occurs in preferential areas while some locations maintain their properties for long periods of time. This concurs with previous results reporting that osteoporotic tissue is quantitatively deficient (low in volume), but remains qualitatively normal.[29]

Fig. 4.6 is another example of two different femoral sections taken from the same cadaver. These images demonstrate two things: the dynamic differences that can be observed from intracadaveric comparisons and the results of a circular averaging technique. A technique was developed by which the circular cross section was divided into 36 radial sections by calculating the properties of the bone at every 10°.[28] An algorithm was then used to calculate a weighted pixel acoustic impedance based on the acoustic properties of all the pixels that surround an individual pixel. The distance between the periosteum to the endosteum was divided by three and the pixels that fell within the three locations were averaged to generate periosteal, middle, and endosteal impedances. A total average was also calculated. Again, significant differences in properties were observed in the endosteal and periosteal locations of the osteoporotic specimen. These results were accentuated by the graphs of the acoustic properties presented on the right. The values on the y axis represent the acoustic impedance on a 0 to 256 scale.
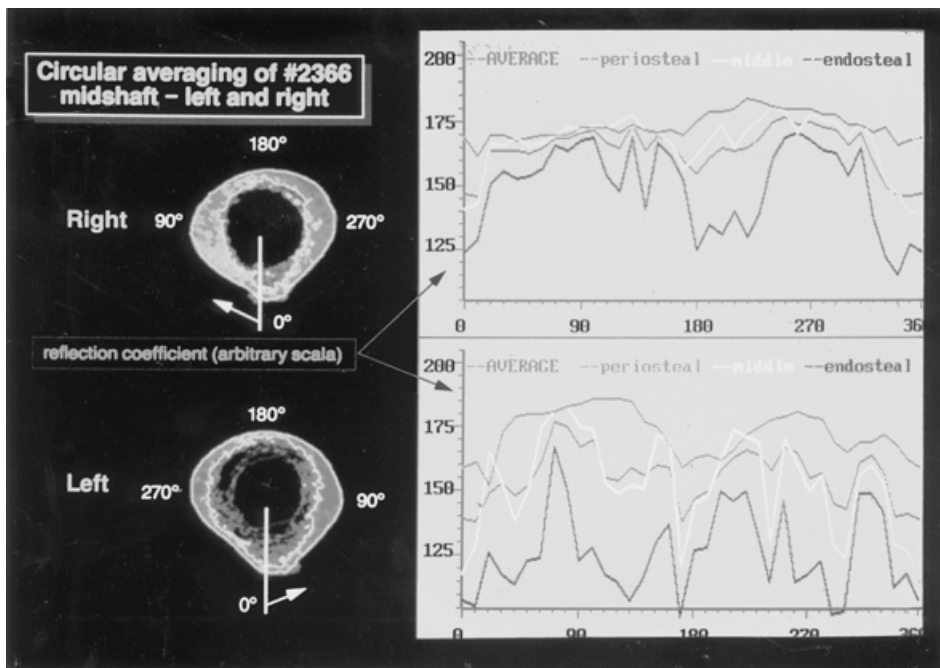
FIGURE 4.6 Two transverse cross sections taken from the same cadaver at the same level. This image demonstrates the variation that can be observed within the same individual. It also highlights the "circular averaging" technique developed by Meunier et al. There is a greater degree of variation observed for bone from different regions within the osteoporotic cross sections. The other section has a less erratic pattern of bone properties.

The right section shows that the periosteal, middle, and average values are relatively constant across the specimen with a decrease in the posterior location of the femur. It is interesting to note that the endosteal properties of this bone have a more irregular pattern and there is a fairly large decrease in the anterior endosteal zone. The porotic femur reveals a much more erratic image, with both the endosteal and middle properties varying widely across the specimen. The average also follows this volatile nature of the middle and endosteal values. Also of note is the general shift of the curves in the direction of reduced properties for the porotic section. This relatively simple technique of identifying the properties within different locations of the section provides a powerful graphic image of the range of remodeled acoustic properties that occur in a diseased state.

In the second study, twenty pairs of human femora were sectioned and scanned.[28] The forty femora were also tested fresh and were sectioned with a diamond saw. Only one section was prepared from the midshaft of the diaphysis of each. The acoustic properties were measured using both a reflection acoustic microscope and a well-published transmission ultrasound technique.[26] Four quadrants from each specimen were evaluated as in the previous study (anterior, posterior, medial, and lateral). The acoustic scanner was slightly different from the one used in the aforementioned system in that a 30 MHz transducer was used. As shown in Fig. 4.7, a second order relationship was established for the reflection coefficients and the elastic stiffness coefficients. An r value of 0.99 demonstrated an excellent agreement between these techniques. This finding coupled with the results shown in Fig. 4.1 presents a strong argument that acoustic impedance is directly related to a material property of bone. The elastic stiffness coefficients are used in the calculation of Young's modulus,[30] and in this case, C_{33} is the most important coefficient in the calculation of Young's modulus.
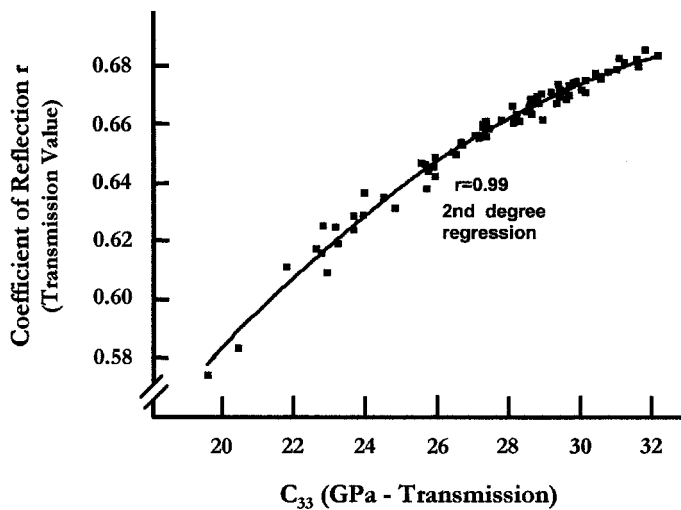

FIGURE 4.7 The relationship between the reflection coefficient and the elastic stiffness coefficient for human femoral bone.[28] An excellent correlation was observed, $r^2 = 0.99$.

Finally, in a most recent study, the relationship between impedance and modulus was tested.[31] Bovine bone was machined and soaked in solutions varying concentrations of NaF. It is hypothesized that the flouride ions replace the hydroxide (OH^-) ions within the hydroxyapatite mineral component of bone. In all, 27 bovine bone specimens were machined from the medial and lateral quadrants of the central 10 mm of each femur. The specimens were formed into flattened dumbbell shapes. The bones were then separated into 50 cc of one of four treatment solutions. Group 1 (n = 6) samples were placed into a solution of 0.145 M NaCl, Group 2 (n = 6) solutions contained 0.145 M NaF, Group 3 (n = 6) solutions contained 0.5 M NaF, and Group 4 (n = 9) solutions consisted of 2.0 M NaF. The samples were set in a water bath shaker for 3 days at 37°C. Fluoride content and density were measured after treatment.

The specimens were mechanically tested to failure in tension. Under constant irrigation with their respective solutions, tests were performed under stroke control at a strain rate of 2.65×10^3 s^{-1}. Deformation was measured using an extensometer with a gage length of 12.5 mm. The specimens were then prepared for SAM analysis. Two scans were made from the gaged length of each specimen in a deionized water bath at room temperature. The images generated had a pixel size of 20 μm. The average impedance of each cross section was measured.

The data demonstrated a good correlation between Young's modulus and acoustic impedance. The mean impedance and modulus for each specimen are plotted in Fig. 4.8. The results were best described

$$Y = 0.113X + 5.590 \ (r^2 = 0.672)$$
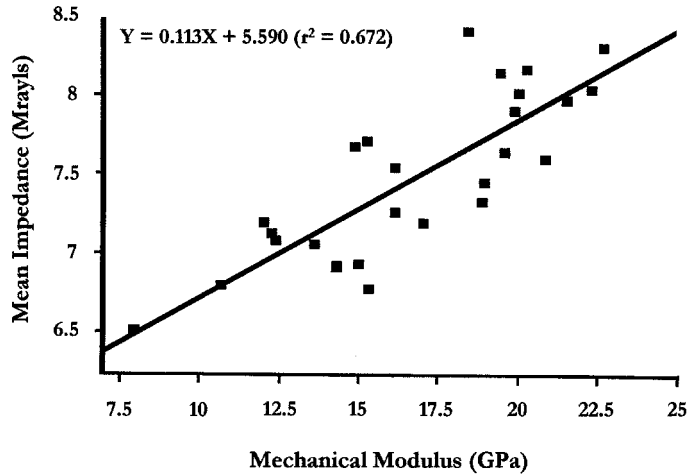
FIGURE 4.8 A graph of the mean acoustic impedance vs. the Young's modulus for bovine bone that has been soaked in solutions of varying concentrations of sodium fluoride.

by a linear relationship with an $r^2 = 0.672$. Increasing concentrations of NaF were seen to result in concomitant decreases in modulus and impedance. The NaF treatments appeared to affect the bone stiffness by diffusing into the samples and altering the bone mineral. This was evident in the SAM images, in which a border of bone with decreased impedance surrounded a core of bone with normal acoustic properties. The width of this border was greater with increasing concentrations of NaF. In fact, with 2.0 *M* NaF, many samples were completely and uniformly penetrated.

Although the relationship is not quite as strong as was observed for the elastic stiffness coefficient in Fig. 4.7, this experiment further supports the relationship between the acoustic impedance and the mechanical properties of bone. Two factors that may have played a role in this weaker relationship include eight other elastic stiffness coefficients are not taken into account with respect to the impedance in one direction; and only two sections within an entire gage length of bone were tested. Additionally, variations in the bone material within the gaged lengths would have also existed. These variations would arise due to the naturally occurring heterogeneities of the bone itself, as well as local differences in flouride ion penetration.

High Frequency

The initial studies were performed using the Olympus UH3. on canine femoral cortical bone.[18] Specimen preparation was performed as described above. Fig. 4.9a is a SAM micrograph obtained of a cortical area of a canine femur cut transverse to the bone axis using a 400 MHz burst mode lens (resolution 3.5 μm) over a 1 mm lateral scan width. Three important new findings were observed. First, the outermost lamellae of each Haversian system (secondary osteon) had the darkest gray levels. The dark gray level here implies lower density and/or elasticity; light gray level implies higher density and/or elasticity. Second, wherever two or more adjacent osteons were abutting, the gray levels of their outermost lamellae appeared to interdigitate. Finally, within an osteon all the lamellae did not have the same gray levels.

Indeed, Fig. 4.10a is a higher frequency scan of the osteon seen in the lower left-hand portion of Fig. 4.9a, and the gray levels of the outermost lamellae are the darkest, while the interior lamellae appear to vary between light and dark, implying variations in density and/or elasticity in adjacent lamellae (600 MHz burst lens, resolution 1.7 μm, lateral scan width 250 μm). Similarly, Fig. 4.11a is a triangular-like intersection of the three osteons indicated by the junction of the arrows seen on Fig. 4.9a (600 MHz burst lens, resolution 1.7 μm, lateral scan width 100 μm). The interdigitation overlap of the darkest gray levels is clearly seen, implying overlap of density and/or elastic properties.
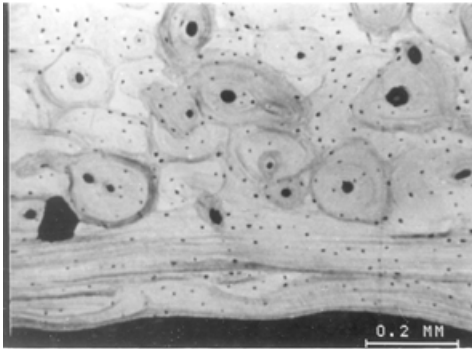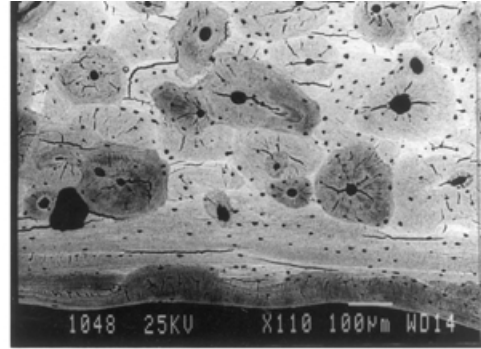
(a)   (b)

FIGURE 4.9a 400 MHz (aperture angle 60°, burst mode, full scale x dimension is 1 mm) SAM micrograph of a portion of canine femoral cortical bone cut transverse to the bone axis. Of particular interest is the lower reflectivity (darker shade of gray) observed for the outermost lamellae of each Haversian system.

FIGURE 4.9b Backscattered electron SEM micrograph of the same region shown in Fig. 4.9a (cracks are drying artifacts). The Haversian systems are well defined and separated from neighboring Haversian systems.
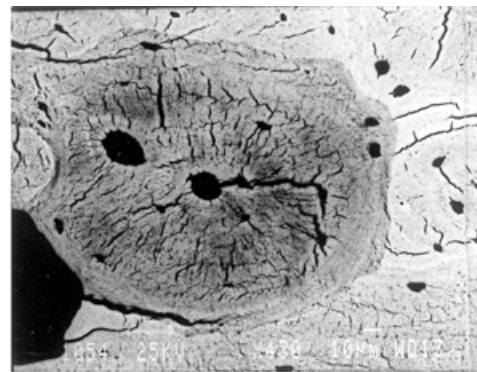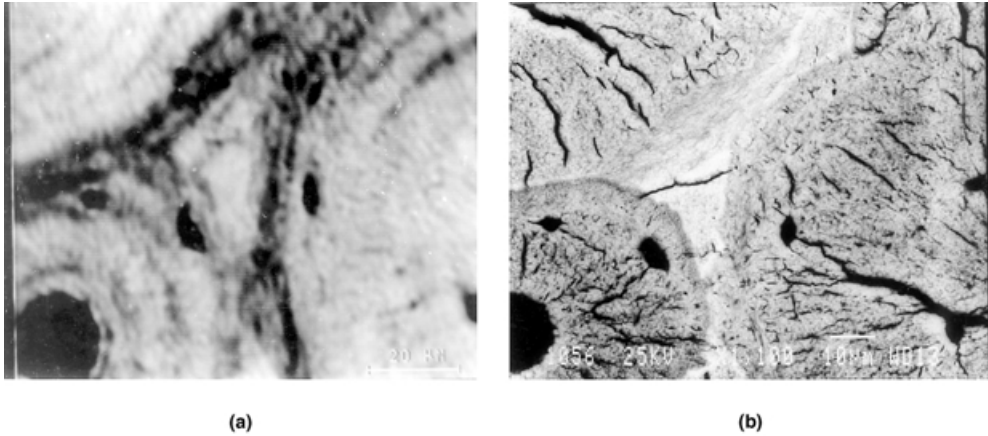

(a)   (b)

FIGURE 4.10a 600 MHz (aperture angle 120°, burst mode, full scale x dimension is 250 μm) SAM micrograph of a large Haversian system in lower left quadrant of Fig. 4.9a clearly showing the lower reflectivity of the outermost lamellae and the apparent interdigitation of gray levels in the upper right corner. The second lumen slightly above and to the left of the Haversian canal appear to be a second canal based on the appearance of lamellae surrounding the opening.

FIGURE 4.10b Backscattered electron SEM micrograph of the same region shown in Fig. 4.10a. The Haversian system is well defined and separated from its neighboring Haversian systems.

To determine whether these outermost lamellae do indeed belong to distinctly different osteons, a second technique delineating structural features must be used. In this case, backscatter scanning electron microscopy (BSEM) was chosen. In the rush to make the structural observations, the proper drying procedures to limit cracking artifacts were not used. Fortunately, the crack artifacts do not obscure the structural information as seen on Figs. 4.9b, 4.10b, and 4.11b, the BSEM micrographs of the same areas seen on the SAM micrographs, Figs. 4.9a, 4.10a, and 4.11a, respectively. It is clearly seen on the SEM micrographs that the osteons are structurally distinct but their outermost lamellae gray levels do indeed interdigitate.

(a)   (b)

FIGURE 4.11a   600 MHz (aperture angle 120°, burst mode, full scale x dimension is 100 mm) SAM micrograph of the selected area between three Haversian systems located at the intersection of the arrows in the lower right quadrant of Fig. 4.9a. The reflectivities of the outermost lamellae of each Haversian system are seen to be comparable, creating what appears to be an interdigitation of these lamellae even though the backscatter electron SEM (Fig. 4.1b) clearly indicates each Haversian system to be distinct and separated from its neighbors.

FIGURE 4.11b   Backscattered electron SEM micrograph of the same region shown in Fig. 4.11a. The Haversian systems are well defined and separated.

These observations on canine bone indicated that it was imperative to perform a similar study on fresh human femoral cortical bone.[18] Fig. 4.12a is a SAM micrograph of a specimen of human femoral cortical bone described by Katz and Meunier[18] (600 MHz burst mode lens, resolution 1.7 µm, lateral scan width 1 mm). Fig. 4.12b is the B SEM micrograph of the same area seen on Fig. 4.12a. Proper drying techniques were used so that crack artifacts were held to a minimum. The same three critical observations made in the canine bone study were made for human bone as well. Indeed the variations in gray levels in alternate lamellae can be observed more dramatically in Fig. 4.13a which is a dark elliptically shaped osteon in the upper left-hand quadrant of Fig. 4.12a (600 MHz burst mode lens, resolution 1.7 µm, lateral scan width 250 µm).

In order to ensure that the specimen surface is both free of gross irregularities and is aligned properly with respect to the lens, a special type of SAM image is run, a so-called x-z image. Here, the lens is defocused a fixed distance, z, below the surface and is then moved upward in the z direction while vibrating along a line in the x direction. This provides an acoustic interference profile in the x-z plane that is due to the interaction of the surface and longitudinal acoustic waves providing acoustic information that can be related to the specimen's elastic properties along the scanned line.

Fig. 4.13b is an x-z SAM micrograph with the same 600 MHz lens taken along the line shown on Fig. 4.13a. The small variations in width of the band reflect the variations in elastic properties among the alternating lamellae as well as possible small height artifacts caused during the polishing process. A calibration system has been developed using a number of materials whose impedance values vary over a wide enough range of values to allow for obtaining elastic moduli for materials varying from low impedances as in soft tissues and polymers to high impedances as in metals and ceramics.
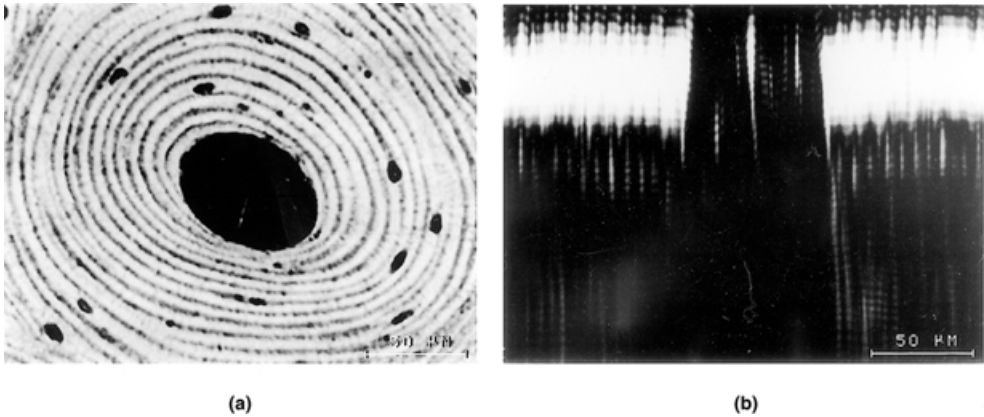
The gray level variations of alternating lamellae observed in cortical bone were also seen in trabecular bone. Fig. 4.14a is a SAM micrograph of a portion of cancellous bone from a sheep femoral condyle (600 MHz burst mode lens, resolution 1.7 µm, lateral scan width 250 µm). Fig. 4.14b is a SAM micrograph taken with the same lens over a lateral scan width of 100 µm showing the region surrounding the lunate-shaped defect seen in the lower left-hand corner on Fig. 4.14a. Not only are the variations in gray level observed, but the effect of the defect on lamellar organization and properties is also clearly delineated.

(a)   (b)
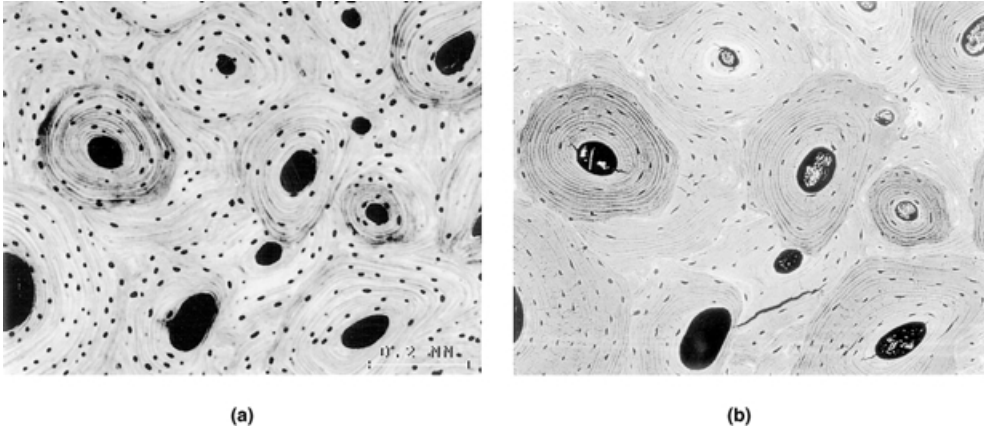
FIGURE 4.12a   600 MHz (aperture angle 120°, bust mode, full scale dimension is 1 mm) SAM micrograph of a portion of human femoral cortical bone cut transverse to the bone axis. The same reduced gray levels of the outermost lamellae and their apparent interdigitation as seen for the canine bone (Figs. 4.9a, 4.10a, 4.11a) are observed here also.

FIGURE 4.12b   Backscattered electron SEM micrograph of the same region shown in Fig. 4.12a. The same clear delineation of individual Haversian structures observed for canine bone (Figs. 4.9b, 4.10b, 4.11b) is observed here also.

(a)   (b)

FIGURE 4.13a   600 MHz (aperture angle 120°, burst mode, full scale x dimension is 250 μm) SAM micrograph of the dark Haversian system seen in the upper left-hand quadrant of Fig. 4.12a clearly showing the variations in gray levels of alternate lamellae.

FIGURE 4.13b   x-z SAM image along the line through the mid-point on Fig. 4.13a (full scale x is 250 μm). The level white band shows the sample was flat and well aligned perpendicular to the lens. Slight incursions in the flat surface reflect, in part, polishing artifacts.

The use of high resolution SAM studies on soft tissues is exemplified in Fig. 4.15, a 400 MHz burst mode micrograph of a sheep meniscus taken over a 1 mm lateral scan width. The collagen fibrillar organization is clearly depicted.
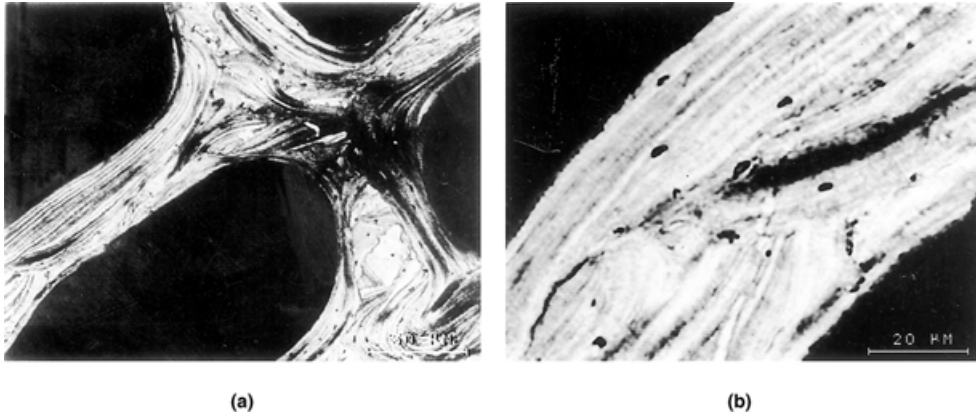
FIGURE 4.14a   600 MHz (aperture angle 120°, burst mode, full scale x dimension is 250 µm) SAM micrograph of a trabecular portion of a specimen of sheep femoral condyle showing clearly the same alternations in gray levels in the lamellar structure as observed in the osteonic lamellae.

FIGURE 4.14b   600 MHz (aperture angle 120°, burst mode, full scale x dimension 100 µm) SAM of the lower left-hand quadrant of Fig. 4.14a. The disruption of the lamellar structure and properties at the tip of the lunate-shaped defect is observed.
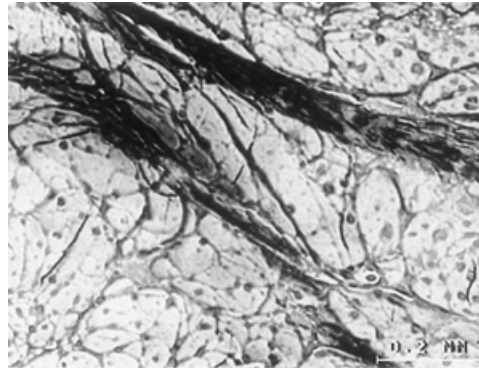
FIGURE 4.15 400 MHz (aperture angle 120°, bust mode, full scale x dimension is 1 mm) SAM micrograph of sheep meniscus showing the collagen fibrillar organization.

4.3   Acoustic Microscopy and Biomaterials Analysis

Acoustic Properties of Remodeled Bone about Metal and Ceramic Coated Metallic Prostheses

Uncemented porous-coated titanium hip implant systems are presently available for total joint arthroplasty. Macrotextured titanium hip implant surfaces have been investigated and include sintered commercially pure titanium (CPTi) beads, diffusion bonded titanium fiber metal pads, and plasma-sprayed CPTi coatings. The purpose of these porous-coated or roughened implant surfaces is to achieve an interlock with the surrounding bone, i.e., the surrounding bone will infiltrate the recesses of the surface macrotexture and provide axial and torsional stability.

To manufacture sintered CPTi beads, layers of spherical CPTi beads are positioned on the femoral component with a binding substance. The femoral component with the applied binding substance–bead mixture is then subjected to the sintering process. Sintering is a high temperature process that dissipates

the binding substance and fuses the beads to each other and to the femoral component. The high temperatures that the femoral component substrate is exposed to can significantly decrease the fatigue strength of the implant system.[32] The strength of the bond of the porous coating to the femoral component substrate is controlled by temperature and length of heating. The porosity is controlled by the sizes of the spherical beads.

Fiber metal pads are produced from wire that has been cut, kinked, and formed in a mold to a specific pattern and shape. The titanium fiber metal pads are positioned into recesses in the femoral component substrate and subjected to the diffusion bonding process. The diffusion bonding process employs the use of heat (lower temperatures than sintering) and pressure application to bond the fiber metal wires to the femoral component substrate.[33] The porosity of the titanium fiber metal pads is controlled by the shape and pattern of the wire.

For the plasma-sprayed CPTi coating, the coating material is heated within a spray nozzle. The coating powder (CPTi) and a pressurized gas mixture are then injected into a high-energy arc created within the nozzle and the molten powder is propelled against the implant surface. The application of a plasma spray coating on titanium alloys also diminishes the fatigue performance of the implant due to the increase in sites for crack initiation and propagation. The characteristics of the plasma sprayed coating are controlled through variations in particle size of the CPTi powder and the pressure applied.

In an attempt to improve the fixation of bone to implants, a key research focus has been the development of surfaces that encourage biological fixation. Bioactive ceramic coatings applied to the surfaces of metallic implants have been intensely investigated.[34-50] Theoretically, a biochemical bond forms between bone and a calcium phosphate ceramic coating, typically hydroxyapatite (HA). Improved implant stability is achieved through this biochemical bond. HA has been shown to enhance the interfacial shear strength and bone contact in animal models when plasma sprayed on a titanium alloy (Ti + 6Al + 4V) implant.[34-44] HA has also been shown to negate the effects, specifically fibrous tissue formation, of an initial surgical gap[45-47,49,50] and micromotion between the bone and implant[48] in animal models. A macrotextured surface with a bioactive coating would have the advantages of enhanced early bone formation and the elimination of fibrous tissue formation, resulting in a strong mechanical fixation with the bone.

The purpose of this study was to investigate arc deposition of CPTi, a new implant surface macrotexturing technique, with AD/HA and a plasma-sprayed HA coating without arc deposition (AD). Multiple analysis techniques were utilized including acoustic microscopy, mechanical testing, qualitative histology, quantitative histomorphometry, and scanning electron microscopy.[51] We will only report on the acoustic microscopy results in this chapter.

Ten purpose-bred coonhounds received staged bilateral hemiarthroplasties in the proximal femurs using the unique Harrington canine femoral component model (HARCMOD HIP). One femur received an uncoated Ti + 6Al + 4V alloy femoral stem with an arc-deposited commercially pure titanium (CPTi) surface. The arc deposition process was achieved by striking an electric arc between two pure titanium wires. A high pressure carrier gas passed through the arc and atomized the melt. This resulted in a spray directed at the alloy substrate. Coating build-up resulted from spatter/cooling of matter spray.

The contralateral femur received a similar stem that had a plasma sprayed hydroxyapatite (HA) coating with a nominal thickness of 50 μm over the CPTi surface. The hydroxyapatite was plasma sprayed onto the surface of the metal. The crystallinity was at least 65% and the coating was 90% pure HA. The surface roughness of the CPTi coating was 30 to 35% greater than the HA coating.

Fig. 4.16 shows the CPTi surface and Fig. 4.17 shows the HA-coated CPTi surface. The femurs were retrieved after 6, 12, and 24 weeks of implantation. The implants were sectioned into seven 6-mm-thick cross sections numbered proximally to distally. Section 4 (center of stem) and section 7 (distal stem) were used for SAM analysis. Fig. 4.18 shows the section locations. Sections were dehydrated in ethanol and embedded in polymethylmethacrylate (PMMA) as previously described.

Twenty-four samples were used for SAM. They were evenly distributed between section 4 and section 7, HA and nonHA coatings, and over the 6-, 12-, and 24-week periods. Samples were ground to a 600 grit finish and scanned with a 50 MHz transducer using an 80 μm resolution and a scanned area of 20 mm × 20 mm. The scanning acoustic microscope was calibrated as previously described.
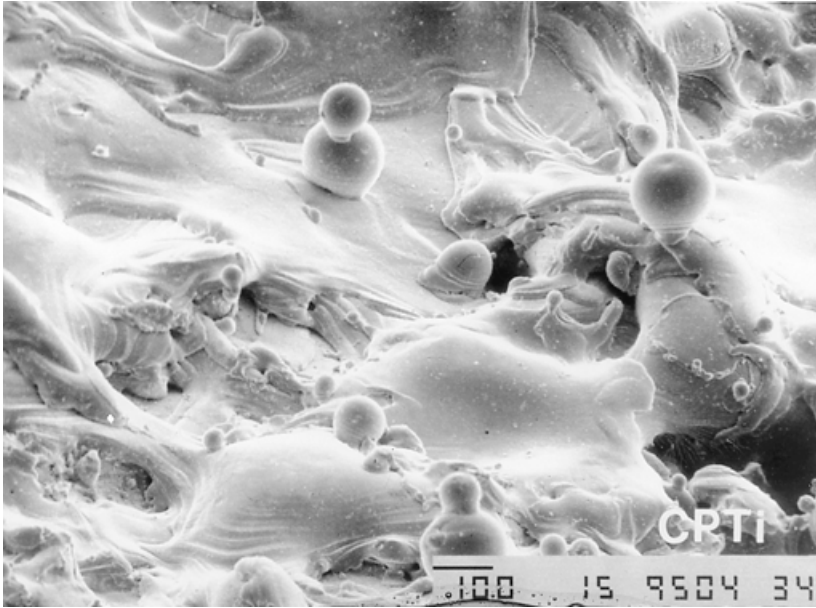
FIGURE 4.16 Secondary electron imaging (SEI) scanning electron photomicrograph of an unimplanted AD surface taken at an angle of 50° in order to show surface topography. Original magnification × 75.
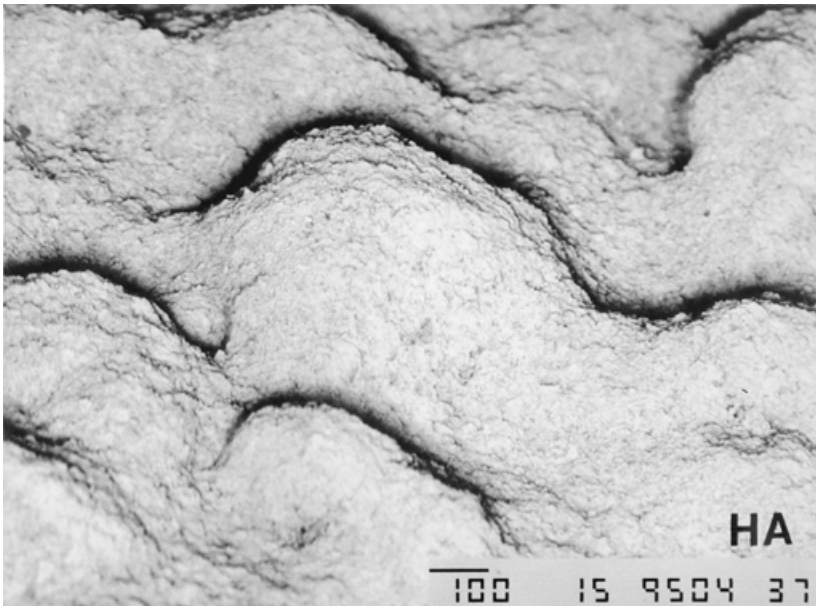

FIGURE 4.17 Secondary electron imaging (SEI) scanning electron photomicrograph of an unimplanted AD/HA surface taken at an angle of 50° in order to show surface topography. Original magnification × 75.

Thresholds were set that eliminated signals from metal and PMMA during analysis. Impedance measurements were taken of (1) the entire sample, (2) the anterior, posterior, medial, and lateral cortical bone regions, and (3) periosteal bone regions when they were present. One-factor analysis of variance (ANOVA) was performed to compare the impedance of the entire sample with respect to implantation time, femoral position of the implant, and surface treatment. A one-factor ANOVA was also performed
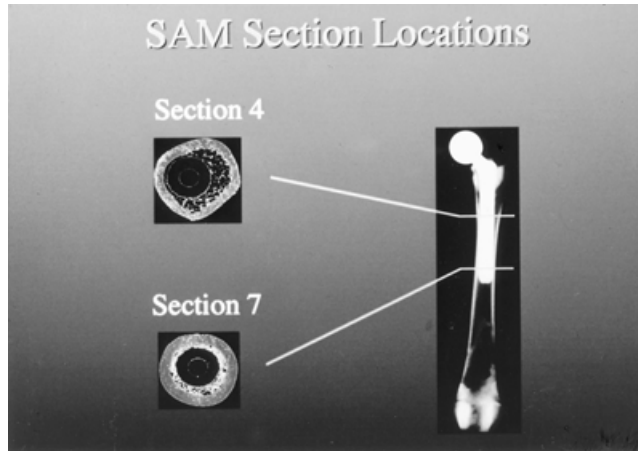
FIGURE 4.18 Schematic implanted specimen indicating sectioning levels for acoustic microscopy.

to test the significance of quadrant location (anterior, posterior, medial, and lateral) on the impedance of cortical bone. A paired t-test was performed to compare the impedance of cortical and corresponding periosteal bone.

The mean acoustic impedance of the canine femoral bone from all of the implant specimens was 8.74 ± 0.25 MRayl. A graph of bone impedances (means) for different implantation times is shown in Fig. 4.19. No statistical difference was found in total impedance between section 4 and section 7 or between HA coated and uncoated CPTi surfaces when analyzing all of the data grouped together. There was a significant difference between the 6-week (8.58 ± 0.35 MRayl) and 24-week (8.87 ± 0.14 MRayl) periods (N = 24, p-value = 0.0214). The difference at the 12-week period (8.77 ± 0.14 MRayl), however, was not statistically significant. A one-factor ANOVA (N = 96) of the cortical bone measured at the four quadrant locations showed a statistically significant difference between posterior (8.82 ± 0.35 MRayl) and anterior (9.04 ± 0.32 MRayl, p-value = 0.0452), posterior and medial (9.06 ± 0.44 MRayl, p-value = 0.0296), and posterior and lateral (9.07 ± 0.38 MRayl, p-value = 0.0208) quadrants. Four of the samples exhibited periosteal bone growth and a paired t-test (N = 4) showed a statistically significant difference between cortical bone impedance (8.62 ± 0.47 MRayl) and periosteal bone impedance (7.09 ± 0.59 MRayl, p-value = 0.0034). Eight transverse cross sections taken from normal canine femora (4 from section 4 and 4 from section 7) had average impedances of 9.34 MRayls.

Fig. 4.20 shows a typical acoustic scan of the canine bone. The implant is located in the center of the medullary canal and trabecular bone struts can be observed bridging the gap between the cortical bone and the implant. This bone has lower acoustic impedance in the range of 6 to 7 MRayls. The histogram highlights the range of properties. The cortical bone has relatively high impedance (greater than 9 MRayls) and there is evidence of remodeling in the posterior quadrant as well as the endosteal area of the bone.

The results of this study demonstrated a significant increase in canine femoral bone impedance around a Ti stem between 6 and 24 weeks post-implantation, suggesting a greater bone stiffness at 24 weeks. This experiment also demonstrated that the acoustic properties of canine femoral bone after implantation of a hip stem differ by position within the bone. The impedance of the posterior region was shown to be less than that of the anterior, medial, and lateral regions. This latter finding is consistent with the work of Ashman et al.[26] who demonstrated a decrease in C_{33} and density in the posterior regions of human and canine femurs as compared with the other quadrants of the bone. No differences in total sample impedance or sample quadrant impedance were observed when comparing samples from section 4 with those of section 7. Moreover, no difference in impedance was shown between HA and uncoated CPTi specimens.

Fig. 4.21 highlights changes in the cortical thickness of the same canine femora that were scanned. A significant reducton in cortical thickness was observed while the average impedance increased. This is a very interesting result that demonstrates how bone remodeling can result in a net decrease in material
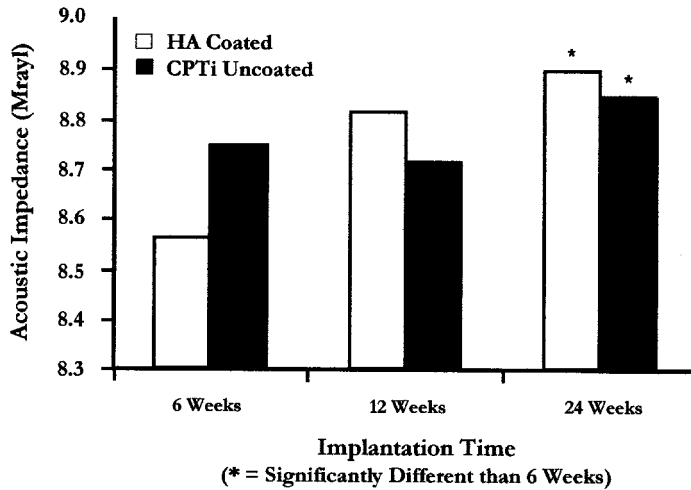
FIGURE 4.19 Graph showing impedance vs. implantation times for CPTi and HaCPTi implants.
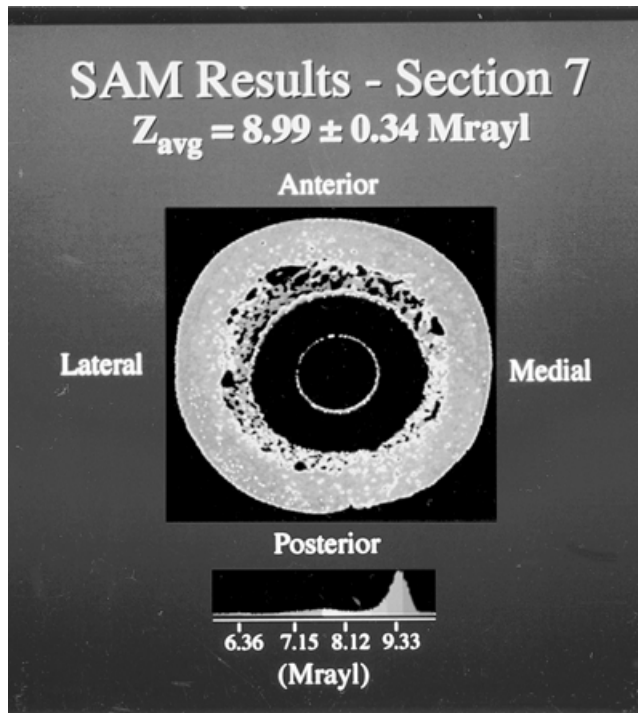

FIGURE 4.20 Typical acoustic scan for a CPTi implant with trabecular bone struts bonding the implant to the bone. The reduced impedance properties of the bone struts are obvious with the cortical bone having more mineralized bone with greater impedance.

yet the properties of the material can remain the same or increase. While cortical thickness reflects a change in volume, the increase in impedance reflects increased calcification and maturation of the bone. This result can be confusing because new intramedullary bone formed within the canal and adjacent to the implant would certainly mature with time and would also affect the average impedance of the section.
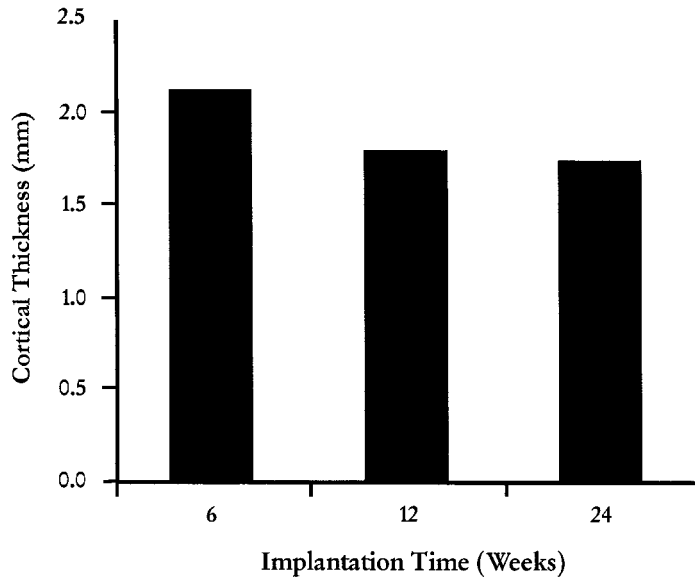
FIGURE 4.21 Mean cortical bone thickness at 6, 12, and 24 weeks for lumped data for AD/HA and AD implants.

## The Analysis of Bone Remodeling Adjacent to Absorbable Polymers

Synthetic degradable polymers are currently under investigation for orthopaedic applications ranging from small bone fixation pins to scaffolds for tissue engineered bone regeneration. While traditional histological, microscopic, and microradiographic techniques yield important insights into the host bone response, they are not able to reveal the effects the polymers may have on the mechanical properties of the bone local to the implant site. In this experiment, scanning acoustic microscopy was used to nondestructively and quantitatively assess the micromechanical properties of bone growing adjacent to poly(L-lactic acid) (PLA) and tyrosine-derived polycarbonate implants.[52]

PLA is biocompatible in the short term, and able to provide adequate strength and stiffness for use in small bone fixation.[53-55] However, PLA implants have been associated with late inflammatory and bone resorption responses.[55] Concerns have been raised regarding the acidic nature of the degradation products and the particulate debris formed during erosion.[56,57] Tyrosine-derived polycarbonates are part of a newly synthesized class of degradable polymers.[58-60] Like PLA, these materials are based on natural metabolites (the amino acid, tyrosine), have favorable mechanical properties, are readily processible, and degrade on the order of months to years. Unlike PLA, tyrosine-derived polycarbonates are completely amorphous. Hence, degradation to crystalline particulate debris is not of practical concern for these materials. Similarly, the degradation products of tyrosine-derived polycarbonates are nonacidic. *In vitro* cytotoxicity[58] and short-term *in vivo* evaluations in rats[61] and rabbits[62] have shown tyrosine-derived polycarbonates to be generally biocompatible. Poly(DTE carbonate) (molecular weight = 121,000) and poly(DTH carbonate) (molecular weight = 220,000) were synthesized according to previously published procedures.[54] Medical grade PLA (molecular weight = 191,000) was obtained from Boehringer Ingelheim in pellet form and used as delivered.

The canine bone chamber model employed in this study and corresponding histological and radiographic findings have been previously described.[63] Briefly, compression molded coupons were fit into a polyethylene bone chamber housing to create 10 ingrowth channels $1 \times 5 \times 10$ mm. Assembled chambers were implanted in a cortical defect created in the lateral metaphysis of the distal femur. Chambers from three dogs at 6-, 12-, 24-, and 48-week time points were analyzed. This yielded two chambers per polymer per time point. The retrieved chambers were fixed, imbedded, and polished as previously described. The

specimens were cut perpendicularly through the centers of the bone chambers and the exposed faces polished for SAM analysis.

The mean impedance of the bone that had penetrated the channels of the bone chambers is summarized in Fig. 4.22. No appreciable difference in the properties of bone growing adjacent to the different polymers was noted at the first three time periods (6, 12, and 24 weeks). All chambers demonstrated good bone ingrowth and a trend toward increasing impedance. However, 48 weeks post-implantation there was a marked decrease in the impedance of the bone in the PLA chambers in comparison to the 24-week PLA data. This was in direct contrast to the bone growing near the tyrosine-derived polymers which was still increasing in impedance at 48 weeks.
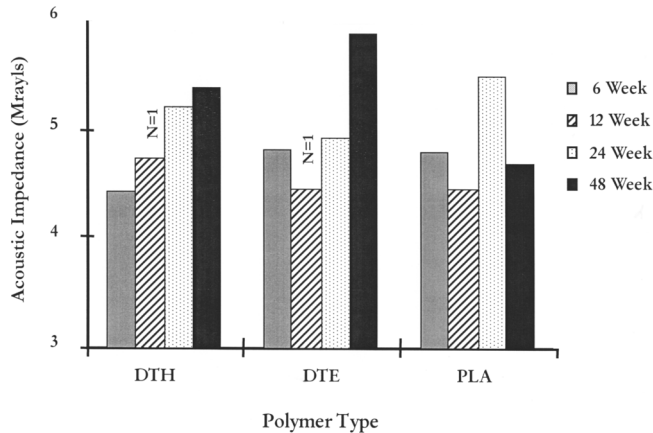
FIGURE 4.22 Bone chamber impedance for poly DTE, poly DTH, and PLA from canine femoral specimens at 6, 12, 24, and 48 weeks.

Figs. 4.23 and 4.24 show acoustic scans of 48-week bone chambers for PLA and PolyDTE, respectively. Very little bone is observed growing into the PLA chamber and the impedance is significantly lower than the impedance at 48 weeks for polyDTE. In contrast, well-mineralized bone is observed filling the channels of the DTE bone chamber.

Using acoustic microscopy, a quantitative micromechanical analysis of bone growing adjacent to biodegradable polymers was possible. The decrease in the elastic properties of the bone juxtaposed to PLA from 24 to 48 weeks possibly reflects the effect of PLA degradation products. Hypothetically, PLA degradation results in a more acidic local environment, causing bone resorption (seen histologically) and consequently a reduction in the impedance of the surrounding bone. On the other hand, bone growing into the tyrosine-derived polycarbonate implants continued to calcify out to 48 weeks and approached 75% of the impedance for normal canine cortical bone.

4.4   Acoustic Microscopy of Partially Mineralized Tissues

Problems and Obstacles in the Mechanical Characterization of Incompletely Calcified Tissues

Classically, the mechanical behavior of bone has been determined for consistent and relatively homogeneous specimens machined or otherwise shaped from diaphyseal compact bone.[64-66] Such samples are typically subjected to tensile or compression tests. This methodology works quite well for the characterization of this type of bony specimen. However, the properties thusly determined are by definition averaged over the specimen's entire cross section and length. Similar testing protocols have been implemented for cores of cancellous bone[67,68] and individual trabeculae.[69,70] While this research provides useful
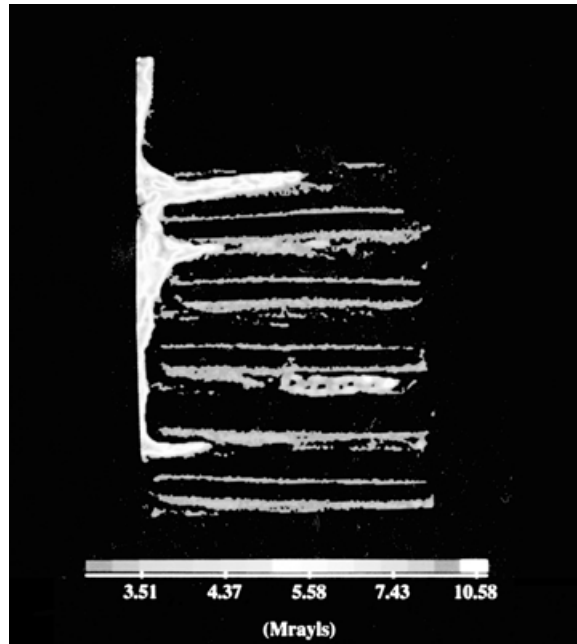
FIGURE 4.23 Typical acoustic scan for a 48-week PLA implant. Relatively little bone is found within the chamber and the impedance is significantly lower.
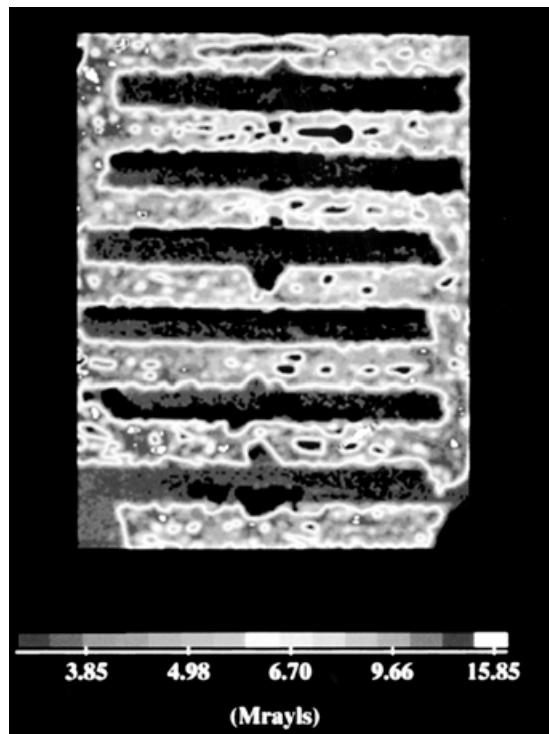
FIGURE 4.24 Typical acoustic scan for a 48-week polyDTE implant. A well-mineralized bone is found adjacent to the polymer coupons.

and important information, these techniques are inherently unsuitable for the investigation of bone formed in rapidly remodeling environments.

The tissue in such instances is highly heterogeneous and anisotropic. Conventional testing procedures that measure bulk specimen properties cannot easily deal with this type of specimen. Bone has a very irregular and delicate structure, making the fabrication and testing of specimens difficult. Numerous researchers have attempted to overcome these obstacles using other techniques. Spatial variations in material hardness can be investigated using a host of indentation tests (Vickers, Brinell, and Rockwell). Each technique uses indentors of a particular size and geometry, from which a measure of material stiffness can be determined. Several investigators[71,72] have successfully used microindentation methods to assess local property variations in various well-mineralized tissues.

Additional research efforts have employed similar methods toward the characterization of local property variations in partially mineralized bone and fracture callus.[21,73,74] While providing information with much greater detail than conventional mechanical testing, the information is gained only for the particular point sampled. The spacing of indents must be rather large due to the effect of each indent on the surrounding area since the material is damaged (work-hardened) for some distance from the point of indentation. The response of the material at the indent site is also dependent on the properties of the adjacent material buttressing the deformed material. Indentation techniques are not well suited for heterogeneous materials. They are also time consuming and cause permanent damage to the specimen.

The mineral density of irregularly shaped and partially calcified bone can also be determined using dual X-ray energy absorptiometry (DEXA). This can be done *in vivo*; however, the resolving capability of most systems is relatively low (approximately 100 μm), and interpreting the results is difficult due to averaging across specimen thickness. Recent advances in micro-computer tomography (micro-CT) have made it possible to evaluate mineralized tissues with complex and irregular geometries with remarkable precision.[75] These systems have been used to reproduce the architecture of cancellous bone as well as lengthened bone segments.

Advantages of Acoustic Microscopy

Using acoustic microscopy one can quickly and easily generate an image in which the contrast is based solely on differing elastic properties, taking into account both material structure and mineral density. When considering calcified tissues in a dynamic state, scanning acoustic microscopy provides numerous advantages. Since it is a graphic technique, it is well suited for evaluating material with a wide range of properties. The gradations and trends in elastic properties are readily apparent throughout the images. Additionally, no specimen processing is necessary other than embedding and sectioning, so an *in situ* evaluation of the tissue properties can be attained. Measurement of acoustic properties in irregularly shaped areas is another great strength of this technology.

In contrast to micro-CT and DEXA, the images generated using scanning acoustic microscopy (SAM) are based on both mineral density and tissue ultrastructure. Therefore, the images are representative of the elastic behavior of the bone. Additionally, a much greater resolution is possible using SAM, and the acoustic information gathered constitutes a surface property measurement, not an average over a thickness as is the case with the volume elements used in micro-CT. Alone or in conjunction with other methodologies, SAM provides a unique way to gain insight into the development of dynamically remodeling environments.

Regional and Temporal Changes in the Acoustic Properties of Fracture Callus in Secondary Bone Healing

In secondary bone healing, the fracture callus provides the limb with temporary stability until the fracture site is replaced with new bone. This process of callus formation involves both intramembranous and endochondral ossification. These two processes occur at different locations and times during the healing process and hypothetically have distinct roles in the restoration of mechanical competence to the skeleton. Thus, the optimum manner in which to evaluate the mechanical properties of fracture callus is not a

clear-cut issue. This is of great concern to the orthopedic investigator because a reliable measure of the mechanical properties of healing bones often plays a pivotal role in the success or failure of many fracture healing studies.

The purpose of this study was to characterize the acoustic properties of healing fractures in normal rats using a scanning acoustic microscope.[76] Unilateral, transverse, and mid-diaphyseal fractures of the right femur were created in 17 Sprague-Dawley rats weighing approximately 400 gm. The animals were sacrificed at 2 (n = 4), 4 (n = 5), 6 (n = 4), and 8 (n = 4) weeks after fracture. Contralateral left femurs were collected from five rats to serve as a control group. The limbs were fixed in 10% buffered formalin and embedded in polymethylmethacrylate (PMMA). Mid-sagittal sections were prepared and analyzed using acoustic microscope.

Each acoustic image was partitioned into six non-overlapping regions, three on the anterior surface and three on the posterior surface as depicted in Fig. 4.25. This was done in an attempt to isolate tissue formed through endochondral and intramembranous pathways without including the original cortical bone. The acoustic impedance and area of bone in each of these regions were then measured using our custom software. The normal limbs were analyzed in a similar fashion to determine the properties of intact bone. However, since no fractures were present in the normal bones, the measurements were made by centering the middle region mid-shaft on the femur.
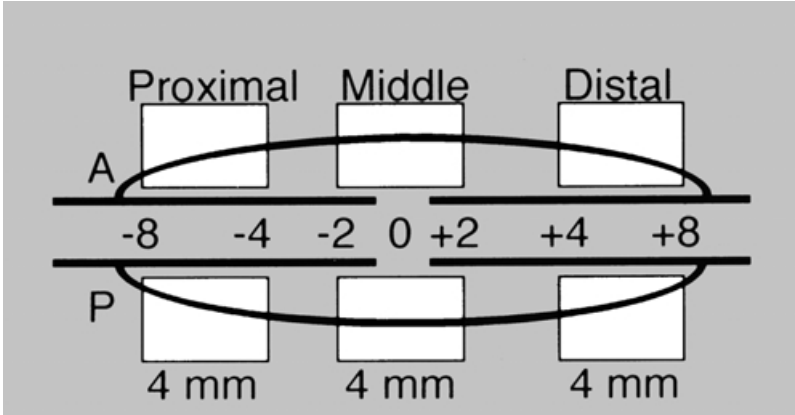

FIGURE 4.25 Idealized fracture callus divided into six regions for the measurement of acoustic properties.

The six regions measured on each scan were used to compute a mean impedance for the fracture callus of each specimen. This was accomplished by calculating a weighted average based on the area of bone present in each of the six regions. Similarly, the mean impedance of the callus in the proximal, middle, and distal locations was determined by computing a weighted average of the two corresponding regions on the anterior and posterior aspects of each limb. These three locations (proximal, middle, and distal) were compared at each time period to determine the regional variations within the callus. The variations occurring within each of these locations with respect to healing time were also examined in order to track the development of bone from specific regions. A single-factor ANOVA was used to analyze the mean impedance of the entire callus at each time period, while a two-factor ANOVA with repeated measures was used to examine the data from the three different regions. When differences were indicated, Bonferroni-Dunn *post hoc* tests were performed at the 95% confidence level to find the significant comparisons.

A significant difference ($p < 0.0013$ for all comparisons) was observed in the mean impedance of the fracture callus from each of the five experimental groups, including the normal femora. Furthermore, the data indicated that an extremely linear relationship ($r^2 = 0.999$) between healing time and mean callus impedance existed as seen in Fig. 4.26. Fig. 4.27 details the regional variations in callus impedance
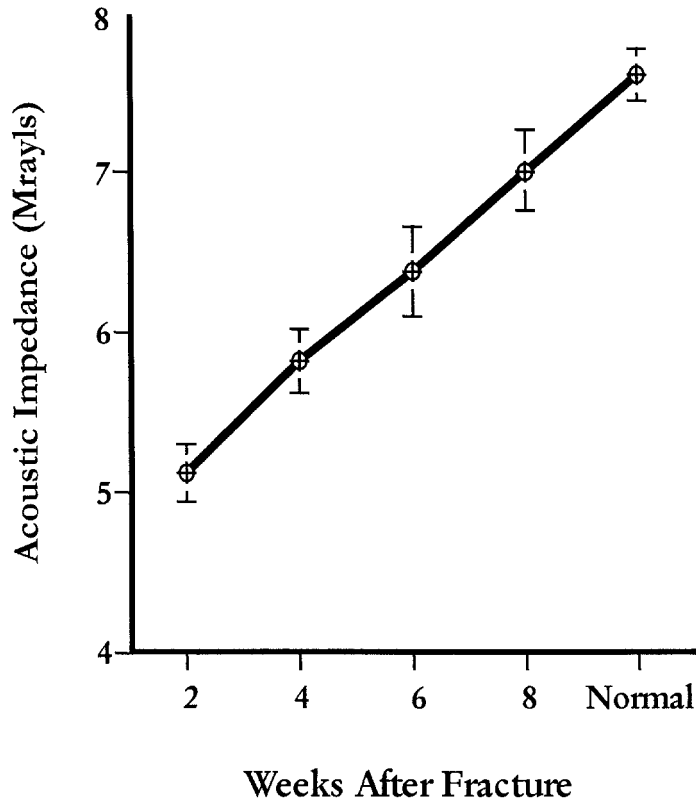
FIGURE 4.26 Mean impedance of fracture callus vs. healing time, demonstrating a nearly linear relationship ($r^2 = 0.999$).

at each time interval. Two weeks after fracture the middle region (4.90 ± 0.13, mean impedance $\pm$ SD) was of significantly lower impedance ($p < 0.0023$) than the proximal region (5.47 ± 0.19). Four weeks after fracture all locations were different, with the proximal (6.59 ± 0.32) having the greatest impedance and the middle (5.44 ± 0.20) having the least. Six weeks post-fracture the proximal callus (7.15 ± 0.35) still exhibited higher impedance values than the middle (6.00 ± 0.30, $p < 0.0017$) and distal regions (6.79 ± 0.13, $p < 0.0106$). However, the middle and distal regions were statistically equal at that time. Eight weeks after fracture, all three regions of the callus were statistically equivalent. Interestingly, the bones of the normal femora exhibited significantly different impedances, $p < 0.012$, in the proximal (7.97 ± 0.18), middle (7.54 ± 0.06), and distal (7.13 ± 0.33) locations.

Evaluating the data by comparing the variations occurring within each region (proximal, middle, and distal) with respect to healing time showed that by 8 weeks post-fracture the impedance of the middle region of the callus was statistically equivalent to the impedance of bone in the middle region (mid-diaphysis) of normal femora. However, at 8 weeks the proximal and distal regions of callus were statistically different from their corresponding regions of normal bone, $p \leq 0.0012$ proximal and $p \leq 0.0021$ distal. Additionally, the 4- and 6-week impedances were found to be statistically equivalent within similar regions, i.e., the proximal region was statistically equal between 4 and 6 weeks.

In the 2-week specimens, no bridging callus was observed using the SAM. The mineralization fronts seen then were of consistently lower impedance than the intramembranous callus. As seen in Fig. 4.28, bridging callus was present in all the specimens in the 4-week group. A broad range of acoustic properties, as demonstrated by the foci of high impedance in Fig. 4.28, was characteristically noted in the middle region of the callus 4 weeks post-fracture. In contrast, the acoustic properties were much more consistent in the callus located further away from the fracture site. Six weeks post-fracture, the acoustic properties
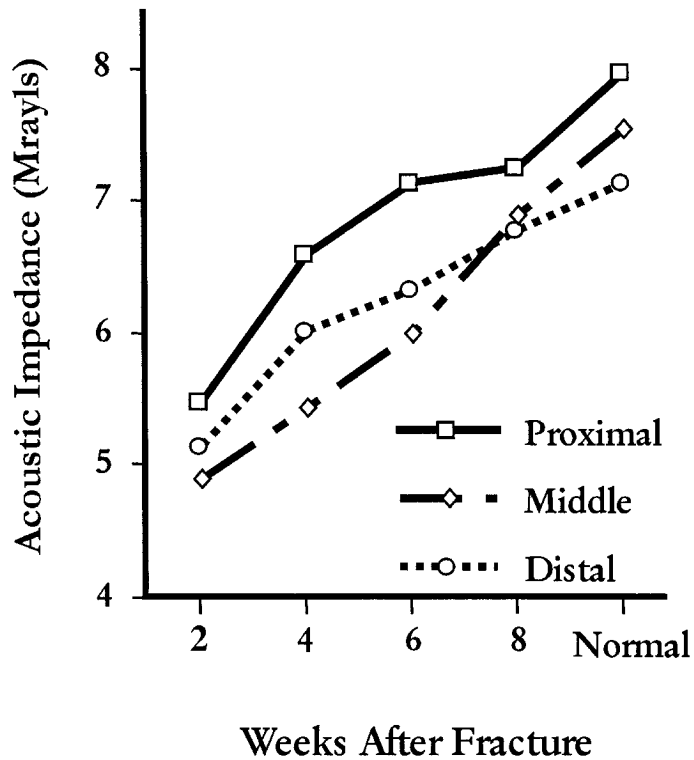
FIGURE 4.27 Acoustic impedance of the various regions (proximal, middle, and distal) within the callus vs. healing time.

of the callus had become much more consistent as remodeling progressed, as demonstrated in Fig. 4.29. The callus of the 8-week group was marked by an even greater uniformity in callus properties and at times was difficult to discern from the bone in the original cortices.

In general, the time course of increasing impedance in the present study is consistent with the changes in the calcium content of fracture callus reported previously in rats[73,77] and in dogs.[74] Although we observed significant differences in the impedance of the callus at each time period, Aro et al.[73] observed that mineralization of the external callus did not change significantly between 3 and 6 weeks post-fracture. In the same study, a similar trend was seen in callus hardness as measured by microindentation. Hardness increased slowly and insignificantly up to 3 weeks, sharply increased between weeks 3 and 4, then did not change between weeks 4 and 6. The model used in that study, however, consisted of bilateral tibial fractures and 0.4 mm stainless steel nails for stabilization. These factors may account for some of the discrepancies with the results presented here.

Millett et al.[78] measured bone mineral density (BMD) in a model identical to the one used in the present study. BMD was measured with a DEXA scanner and an ultrahigh-resolution software package. A significant increase between 2 and 8 weeks but not between 8 and 12 weeks was reported. The mean increase in BMD between 2 and 8 weeks for all sections analyzed was 12.4%. In the present study, the mean increase in acoustic impedance between 2 and 8 weeks in similar regions was 37%. The rather large difference in these two measurements may be a result of the structural changes detected by acoustic microscopy. Significant increases in tissue organization will occur as the fracture site remodels. These changes, as well as mineral density increases, may explain the relatively larger impedance increases seen with the SAM.

Walsh et al.[79] examined the mechanical properties of unilateral fractures in the femora of rats stabilized with 0.45 mm K-wires. A rapid rise in peak tensile load was noted, although 6 weeks after fracture the
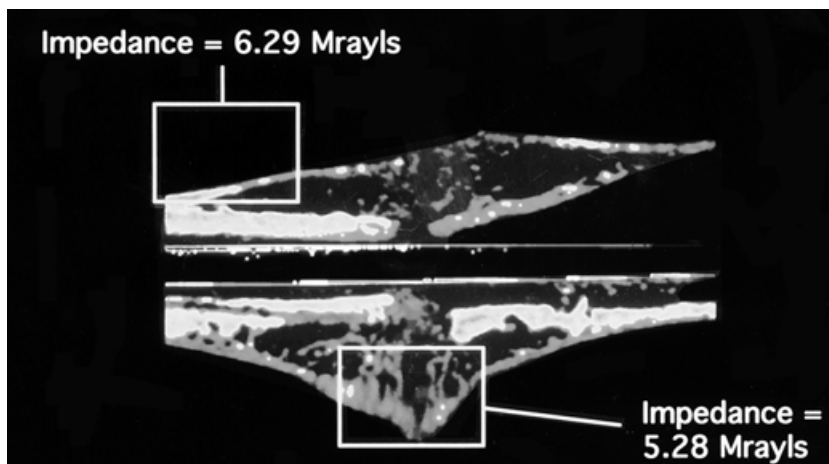
FIGURE 4.28 Acoustic image of a rat femur 4 weeks post-fracture. Boxes indicated foci of high impedance in the callus, illustrating the highly heterogeneous distribution of acoustic properties characteristically seen at this time period.
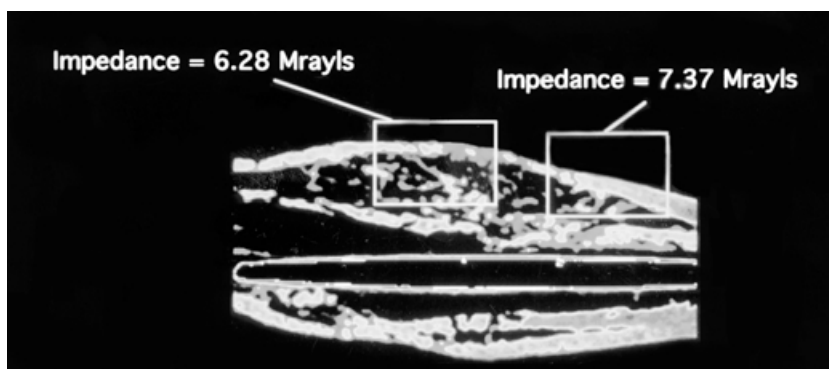
FIGURE 4.29 Acoustic image of a rat femur 6 weeks post-fracture. The formation of a new cortical shell with a wide range of acoustic properties was typically present in the specimens at this time period.

experimental limbs demonstrated only 50% of the tensile force to failure of their contralateral normals. Variables in all of these studies include bilateral vs. unilateral models, presence and size of K-wires for fixation, and the ages and sizes of the animals. To be sure, these factors will have some effect on the outcome, and make direct comparisons between studies difficult. Overall, the relationship between acoustic impedance and healing time seen in the present study was more linear, and had less variation within each time period than any mechanical or physical parameters reported in the literature for a fracture healing model. It is possible that the acoustic properties of these tissues may provide a more representative measure of their development than any previously used techniques.

A unique feature of this study is that the acoustic trends we observed in the different regions may be interpreted based on our histological findings. For example, the impedance of the middle region did not begin to rapidly increase until 4 weeks post-fracture. Histologically, this corresponded to the time period when the middle region was beginning to mineralize. Six weeks post-fracture the impedance of this region (middle) was still rapidly increasing and histologically we observed a much more remodeled callus with the development of woven bone. Thus, by using SAM, it is possible to get some idea of how the various reparative processes contribute to the development of elastic properties within the callus. Since the stability and ultimate healing of fractured bones will be functions of the stiffness of the callus

immediately adjacent to the fracture site, the determination of the acoustic properties in this region may provide a more realistic measure of fracture healing.

In summary, the data in this experiment indicated that during the early stages of fracture healing, callus formed through intramembranous ossification has a more rapid rise in impedance than endochondral callus. However, as the transformation to woven bone takes place, the acoustic properties of the middle portion of the callus (endochondral origin) quickly increased to equal the proximal and distal regions by the eighth week post-fracture. Bronk et al.[80] hypothesized that different mechanical test results (tension vs. torsion) are affected by different healing events. The data presented here may provide indirect evidence in support of their findings.

The ability of the SAM technique to accurately image local acoustic property gradients can be a great strength when studying highly heterogeneous and dynamic environments such as those encountered during fracture healing. As demonstrated in this study, we were able to quantitatively measure variations in the callus from different locations with a precision that to date has not been accomplished. While these results in and of themselves are significant, the proven ability to image and measure these variations may have more widespread implications. Many factors thought to enhance the process of fracture repair, such as growth factors, micromotion, or electromagnetic fields, are likely to have only regionally specific effects which might only be detected with acoustic microscopy.

The Acoustic Properties of Bone Formed during Limb Lengthening

Limb lengthening as the name implies, refers to the clinical practice of increasing the length of the long bones of the skeleton. In contemporary orthopedics, this is nearly synonymous with the process of distraction osteogenesis. This technique was first developed and practiced during the 1950s by Dr. Gavril Ilizarov in Sibera. Briefly, this process involves the steady and slow separation of two bone fragments after the surgical creation of a fracture. An external fixation device is used to provide stability, and a means for gradually increasing the distance between the bone ends via an adjustable mechanism. The actual process of distraction or lengthening ensues after a latency period of a few days to allow for initial healing and callus formation. The new tissue (or bone regenerate) formed in the created gap begins to mineralize from the original bone ends toward the center of the gap. Many factors affect the outcomes of these procedures, and for that reason distraction osteogenesis has become an active area of research in the orthopedic community.

Assessing the mechanical properties of the bone formed during distraction osteogenesis is not an easy task. At the end of distraction, the morphology of the regenerate consists of axially aligned cones, or pyramidal-like projections of bone extending toward an unmineralized fibrous interzone at the center of the gap. The width of this interzone gradually decreases as the regenerate matures. Evaluating the properties of the regenerate is complicated for many reasons. During the early stages of regeneration, there are wide ranges in mineral content, structure, and location. In other words, as seen during fracture healing, bone is a heterogeneous, irregular, and anisotropic tissue. Analyses characteristically are conducted using microradiography and/or various histological techniques, most of which are cumbersome. With an acoustic microscope, it is possible to quantify how the various factors affect the material properties of the new bone, as well as monitor the maturation process. A series of experiments were undertaken to examine the effects of several variables on the acoustic properties of bone formed during distraction osteogenesis.

The first experiment[81] was designed to evaluate the effects of lengthening rate. Unilateral mid-diaphyseal limb lengthenings were performed on the right tibiae of eight skeletally mature, male, New Zealand white rabbits. An Orthofix M-100 mini-lengthener was applied to the anteromedial aspect of each limb. Four animals were lengthened at a rate of 1.4 mm/day, while another four were lengthened at 0.70 mm/day. Half of the animals in each group were lengthened to achieve a maximum length of 14 mm. The remaining animals in each group were sacrificed midway through the lengthening process. The animals from the slower distraction group (0.70 mm/day) had formed new bone with significantly greater ($p < 0.05$) acoustic properties than those subjected to the faster (1.4 mm/day) rate of distraction.

Interestingly, the volume of callus formed was similar between the two groups. It appeared that the slower rate of distraction allowed the bone regenerate to mature more rapidly, although there was no net increase in new bone deposition. A previous study investigating lengthening rates in an identical model concluded that there was no difference in bone formation using the same two rates of distraction.[82] This finding was most likely the result of using qualitative analysis techniques that were unable to discern distinct differences between the experimental groups.

The hypothesis of the second study[83] was that the preservation of the internal blood supply via a corticotomy technique would establish a more favorable environment for limb lengthening, resulting in bone regenerate with greater acoustic properties. Previous studies investigating the importance of preserving the medullary vasculature during distraction osteogenesis have generated conflicting and/or inconclusive findings.[84-86] As in the first experiment, lengthenings were performed on the right tibiae of skeletally mature New Zealand white rabbits using the same hardware and techniques. An osteotomy was performed using one of two techniques (day 0). In Group 1 (18 animals), a simple osteotomy was performed using an air driven oscillating saw. Group 2, consisting of an additional 18 animals received corticotomies. The corticotomy consisted of perforating the tibia with a 1.1 mm drill around its circumference without entering the medullary space. The fracture was completed by gently bending the limb with the fixator loosely applied to prevent excessive displacement of the bone ends.

Ten days after surgery, lengthening was started at a rate of 0.35mm/12h for a period of 20 days in both groups. Weekly radiographs were taken to monitor the lengthening process. At the end of distraction (Day 30), six animals from Group 1 and six animals from Group 2 were sacrificed. Three weeks later (Day 51), six animals from Group 1 and six from Group 2 were sacrificed. The remaining animals were sacrificed three weeks later (Day 72).

As in the previous studies, the limbs were fixed in formalin and embedded in PMMA. The tibiae were sectioned in the sagittal plane, and prepared for evaluation with a scanning acoustic microscope (SAM). Only material located directly in the lengthened gap was included in this analysis to avoid the effects of periosteal callus and original cortical bone. This process was also modified to exclude the effect of the embedding material. Thus, only the impedance of the bone regenerate was determined. The data were analyzed using t-tests and a 0.05% significance level. Comparisons were made between osteotomy methods at each time period and between the three time periods as well.

The mean impedance of the bone regenerate at the end of distraction was 3.74 ± 0.07 MRayls for the corticotomized animals and 3.64 ± 0.03 MRayls for the osteotomized group. These two groups were significantly different ($p = 0.016$). Three weeks post-distraction, the mean impedance of the corticotomized and osteotomized groups was 4.19 ± 0.19 and 4.07 ± 0.64 MRayls, respectively. Three weeks post-distraction, both groups were statistically equivalent. Six weeks post-distraction, the impedance of the corticotomized group was 4.81 ± 0.28, whereas, the osteotomized group impedance was 4.65 ± 0.33. As in the 3-week group, there was not a significant difference in the data at 6 weeks. Despite the lack of statistical significance at 3 and 6 weeks, it is worthwhile to note that the acoustic impedance of the regenerate in the corticotomized series was consistently greater. Pooling the data at each time point showed that the impedance of the regenerate at 3 weeks post-distraction was significantly greater than at the end of distraction ($p < 0.0001$). As a point of reference, the impedance of the normal rabbit tibial cortical bone was observed to consistently have values of approximately 8 MRayls. These results are summarized in Fig. 4.30.

Fig. 4.31 presents typical acoustic images of a limb lengthened corticotomy and osteotomy at the end of lengthening. The corticotomy demonstrates advanced healing with an average acoustic impedance of 4.05 MRayls. The osteotomy has an average impedance that is significantly lower at 3.47 MRayls.

A major shortcoming of most limb lengthening studies is their inability to quantitatively assess the effect of the factors under investigation and the quality of the new bone formed. In the present study, we have quantitatively detected differences in the material properties of the bone regenerate formed as a result of two different corticotomy methods. This is a highly significant finding in limb lengthening research. Previous studies have concluded that complete severing of the endosteal blood supply has little or no impact on distraction osteogenesis.[84-86] The similarity between the two groups at 3 and 6 weeks

Weeks Post Lengthening	Corticotomy	Osteotomy
0*	3.75 ± 0.07	3.64 ± 0.03
3	4.19 ± 0.19	4.08 ± 0.64
6	4.81 ± 0.28	4.65 ± 0.33

* $(p = 0.016)$

FIGURE 4.30 Table of mean acoustic impedances for limb lengthened corticotomies and osteotomies at 0, 3, and 6 weeks post-lengthening.
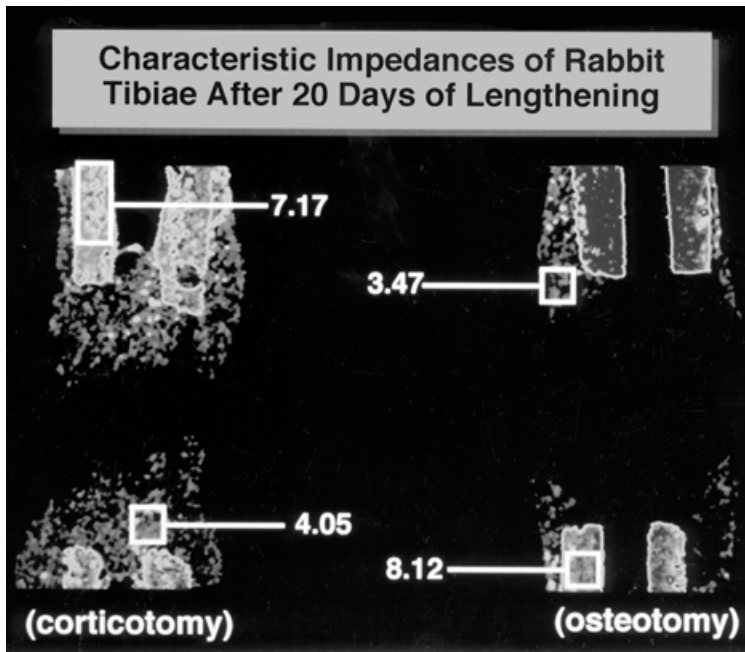
FIGURE 4.31 Acoustic scan of a limb lengthened by corticotomy and osteotomy immediately post-lengthening. Regional variations in impedance are highlighted. The corticotomy callus has greater impedance than the osteotomy callus (4.05 vs. 3.47 Mrayls).

post-distraction is not surprising because the blood supply has most likely been fully restored at this time in the osteotomized animals. The study of regenerate properties at later time periods may yield a more accurate description of the biomechanical development of the bone regenerate than is possible with conventional mechanical testing techniques.

Acknowledgments

References

1. Kolsky, H., *Stress Waves in Solids* , Clarendon Press, Oxford, 1953.
2. Beyer, R. and Lechter, S., *Physical Ultrasonics* , Academic Press, New York, 1969.
3. Lemons, R. and Quate, C., *Appl. Phys. Lett* ., 24, 163, 1974.
4. Jipson, V. and Quate, C., *Appl. Phys. Lett* ., 32, 789, 1978.
5. Gilmore, R., Joynson, R., Trzaskos, C., and Young, J., *Phil. Trans. R. Soc.*, 320, 215, 1986.
6. Kessler, L., *Metals Handbook* , 9th ed., ASME International, Materials Park, OH, 1989, Vol. 17, 465.
7. Bereiter-Hahn, J. and Buhles, N., *Imaging and Visual Documentation in Medicine* , Elsevier, Amsterdam, 1987, 537.
8. Bereiter-Hahn, J., *Scanning Image Technol* ., 809, 162, 1987.
9. Bereiter-Hahn, J., Litniewski, J., Hillmann, K., Krapohl, A., and Zylberg, L., *Acoustical Imaging* , Plenum Press, New York, 1989, 27.
10. Briggs, G., Daft, C., Fagan, A., Field, T., Lawrence, C., Montoto, M., Peck, S., Rodriguez, A., and Scruby, C., *Acoustical Imaging* , Plenum Press, New York, 1989, 1.
11. Lees, S., Tao, N.J., and Lindsay, S.M., *Acoustical Imaging* , Plenum Press, New York, 1989, 371.
12. Okawai, H., Tanaka, M., Dunn, F., Chubachi, N., and Honda, K., *Acoustical Imaging* , Plenum Press, New York, 1989, 193.
13. Kasahara, S., Yoshida, K., Kushibiki, J., and Chubachi, N., *Acoustical Imaging* , Plenum Press, New York, 1989, 153.
14. Meunier, A., Katz, J.L., Kristal, P., and Sedel, L., *J. Orthop. Res* ., 6, 770, 1988.
15. Tatento, H., Iwashita, Y., Kawano, K., and Noikura, T., *Acoustical Imaging* , Plenum Press, New York, 1989, 125.
16. Zimmerman, M., Meunier, A., Kristal, P., Katz, J., and Sedel, L., *J. Orthop. Res.* 7, 607, 1989a.
17. Zimmerman, M., Meunier, A., Katz, J., and Kristal, P*., IEEE Trans. Biomed. Eng* ., 37, 433, 1990.
18. Katz, J. and Meunier, A., *J. Biomechanical Eng* ., 115, 543, 1993.
19. Gardner, T., Elliott, J., Sklar, Z., and Briggs, G., *J. Biomechanics* , 25, 1265, 1992.
20. Hasegawa, K., Turner, C., Recker, R., Wu, E., and Burr, D., *Bone*, 16, 85, 1995.
21. Broz, J., Simske, S., and Greenberg, A., *J. Biomechanics* , 28, 1357, 1995.
22. Turner, C., Chandran, A., and Pidaparti, V., *Bone*, 17, 85, 1995.
23. Pidaparti, V., Chandran, A., Takano, Y., and Turner, C., *J. Biomechanics* , 29, 909, 1996.
24. Briggs, G., *Acoustic Microscopy* , Oxford University Press, New York, 1992.
25. Zimmerman, M.C., Prabhakar, A., Chokshi, B.V., Budhwani, N., and Berndt, H., *J. Biomed. Mater. Res*., 28, 931, 1994.
26. Ashman, R., Cowin, S., Van Buskirk, W., and Rice, J., *J. Biomechanics* , 17, 349, 1984.
27. Bloebaum, R.D., Ota, D.T., Skedros, J.G., and Mantas, J.P., *J. Biomed. Mater. Res* ., 27, 1149, 1993.
28. Meunier, A., Riot, O., Kristal, P., and Katz, J.L*., Interface in Medicine and Mechanics* , Elsevier, London, 1991, 454.
29. Gillespy, T., III and Gillespy, M.P., *Rad. Clin. North America* , 29, 77, 1991.
30. Yoon, H. and Katz, J., *J. Biomechanics* , 9, 407, 1976.
31. Harten, R. Jr., Depaula, C., Kotha, S., Zimmerman, M., Parsons, J., and Guzelsu, N., *Transactions of the 23rd Annual Meeting of the Society for Biomaterials* , New Orleans, 1997.
32. Pilliar, R., *Clin. Orthop* ., 176, 42, 1983.
33. Galante, J., Rostoker, W., Lueck, R., and Ray, R*., J. Bone Jt. Surg* ., 53A, 101, 1971.

34. Thomas, K., Kay, J., Cook, S., and Jarcho, M., *J. Biomed. Mater. Res*., 21, 1395, 1987.
35. Geesink. R., de Groot, K., and Klein, C., *J. Bone Jt. Surg*., 70B, 17, 1988.
36. Rivero, D., Fox, J., Skipor, A., Urban, R., and Galante, J., *J. Biomed. Mater. Res*., 22, 191, 1988.
37. Klein, C., Patka, P., van der Lubbe, J., Wolke, J., and de Groot, K., *J. Biomed. Mater. Res*., 25, 53, 1991.
38. Dhert, W., Klein, C., Jansen, J., van der Velde, E., Vriesde, R., Rozing, P., and de Groot, K., *Biomed. Mater. Res*., 27, 127, 1993.
39. Dhert, W., Klein, C., Jansen, J., van der Velde, E., Vriesde, R., Rozing, P., and de Groot, K., *Biomed. Mater. Res*., 25, 1183, 1991.
40. Bauer, T., Gaisser, D., Uratsugi, M., and Reger, S., *Handbook of Bioactive Ceramics*, CRC Press, Boca Raton, FL, 1990, Vol. 2.
41. Hayashi, K., Inadome, T., Mashima, T., and Sugioka, Y., *Biomed. Mater. Res*., 27, 557, 1993.
42. Jansen, J., van der Waerdan, J., Wolke, J., and de Groot, K., *Biomed. Mater. Res*., 25, 973, 1991.
43. Jansen, J., van der Waerdan, J., and Wolke, J., *J. Biomed. Mater. Res*., 27, 603, 1993.
44. Jansen, J., van der Waerdan, J., and Wolke, J., *J. Appl. Biomaterials*, 4, 213, 1993.
45. Carlsson, L., Rostlund, T., Albrektsson, B., and Albrektsson, T., *Acta Orthop. Scand*., 59, 272, 1988.
46. Soballe, K., Hansen, E., Brockstedt-Rasmussen, H., Penderson, C., and Bunger, C., *Acta Orthop. Scand*., 61, 299, 1990.
47. Soballe, K., Hansen, E., Brockstedt-Rasmussen, H., Hjortdal, V., Juhl, G., Penderson, C., Hvid, I., and Bunger, C., *Clin. Orthop. Rel. Res*., 272, 300, 1991.
48. Soballe, K., Hansen, E., Brockstedt-Rasmussen, H., Jorgensen, P., and Bunger, C., *J. Orthop. Res*., 10, 285, 1992.
49. Maxian, S., Zawadsky, J., and Dunn, M., *J. Biomed. Mater. Res*., 28, 1311, 1994.
50. Dalton, J., Cook, S., Thomas, K., and Kay, J., *J. Bone Jt. Surg*., 77A, 97, 1995.
51. Walenciak, M., Zimmerman, M., Harten, R. Jr., Ricci, J., and Stamer, *J. Biomed. Mater. Res*., 31, 465, 1995.
52. Harten, R. Jr., James, K., Charvet, J., and Zimmerman, M., *Transactions of the 23rd Annual Meeting of the Society for Biomaterials*, New Orleans, 1997.
53. Bostman, O., *J. Bone Jt. Surg*., 73, 148, 1991.
54. Bucholz, R., Henry, S., and Henley, M., *J. Bone Jt. Surg*., 76, 319, 1994.
55. Suganuma, J. and Alexander, H., *J. Appl. Biomaterials*, 4, 13, 1993.
56. Taylor, M., Daniels, A., Andriano, K., and Heller, J., *J. Appl. Biomaterials*, 5, 151, 1994.
57. Daniels, A., Taylor, M., Andriano, K., and Heller, J., *Proc. Orthop. Res. Soc*., 17, 88, 1992.
58. Ertel, S. and Kohn, J., *J. Biomed. Mater. Res*., 28, 919, 1994.
59. Kohn, J., *Drug New Perspect*., 4, 289, 1991.
60. Pulapura, S. and Kohn, J., *Biopolymers*, 32, 411, 1992.
61. Silver, F., Marks, M., Kato, Y., Li, C., Pulapura, S., and Kohn, J., *Long-Term Effects. Med. Implants*, 1, 329, 1992.
62. Ertel, S., Kohn, J., Zimmerman, M., and Parsons, J., *J. Biomed. Mater. Res*., 29, 1337, 1995.
63. Choueka, J., Charvet, J., Koval, K., Alexander, H., James, K., Hooper, K., and Kohn, J., *J. Biomed. Mater. Res*., 31, 35, 1996.
64. Keller, T., Mao, Z., and Spengler, D., *J. Orthop. Res*., 8, 592, 1990.
65. Reilly, D., Burstein, A., and Frankel, V., *J. Biomechanics*, 7, 271, 1974.
66. Reilly, D. and Burstein, J., *J. Biomechanics*, 8, 393, 1975.
67. Goldstein, S., *J. Biomechanics*, 20, 1055, 1987.
68. Kaplan, S., Hayes, W., Stone, J., and Beaupre, J., *J. Biomechanics*, 18, 723, 1985.
69. Townsend, P., Rose, R., and Radin, E., *J. Biomechanics*, 8, 199, 1975.
70. Ryan, S. and Williams, J., *J. Biomechanics*, 22, 1143, 1991.
71. Evans, G., Behiri, J., Currey, J., and Bonfield, W., *J. Mater. Sci.*, 38, 1990.
72. Hodgkinson, R., Currey, J., and Evans, G., *J. Orthop. Res*., 7, 754, 1989.
73. Aro, H., Wippermann, B., Hodgson, S., Wahner, H., Lewallen, D., and Chao, E., *J. Bone Jt. Surg*., 71A, 1020, 1989.

74. Markel, M., Wikenheiser, M., and Chao, E., *J. Orthop. Res*., 8, 843, 1990.
75. Waanders, N., Senunas, L., Richards, M., Steen, H., Schaffler, M., Goldstein, S., and Goulet, J., *Transactions of the 41st Annual Meeting of the Orthopaedic Research Society*, 1995, 567.
76. Harten, R., Lee, F., Zimmerman, M., Hurowitz, E., Arakal, R., and Behrens, F., *J. Orthop Res*., 15, 4, 1997.
77. Aro, H., Wipperman, B., Hodgson, S., Wahner, H., Lewallen, D., and Chao, E., *Transactions of the 34th Annual Meeting of the Orthopaedic Research Society*, 1988, 415.
78. Millett, P., Cohen, B., Allen, M., and Rushton, N., *Transactions of the 42nd Annual Meeting of the Orthopaedic Research Society*, 1996, 623.
79. Walsh, W., Asprinio, D., Sherman, P., Staebler, M., Trafton, P., and Ehrlich, M., *Transactions of the 19th Annual Meeting of the Society for Biomaterials*, Birmingham, AL, 1993, 123.
80. Bronk, J., Ilstrup, D., An, K.-N., Urabe, K., and Bolander, M.E., *Transactions of the 41st Annual Meeting of the Orthopaedic Research Society*, 1995, 587.
81. Harten, R., Zimmerman, M., Weiss, S., and Lee, F., *Transactions of the 21st Annual Meeting of the Society for Biomaterials*, 1995, 345.
82. Yasui, N., Kojimoto, H., Sasaki, K., Kitada, A., Shimizu, H., and Shimomura, Y., *Clin. Orthop. Rel. Res*., 293, 55, 1993.
83. Harten, R., Zimmerman, M., Lee, F., and Alberta, F., *Transactions of the 42nd Annual Meeting of the Orthopaedic Research Society*, 1996.
84. Delloye, C., Delefortrie, G., Coutelier, L., and Vincent, A., *Clin. Orthop*., 250, 34, 1990.
85. Frierson, M., Ibrahim, K., Boles, M., Bote, H., and Ganey, T., *Clin. Orthop*., 301, 19, 1994.
86. Kojimoto, H., Yasui, N., Goto, T., Matsuda, S., and Shimomura, Y., *J. Bone Jt. Surg*., 70B, 543, 1988.
87. Meunier, A., Riot, O., Kristal, P., and Katz, J.L., *Interface in Medicine and Mechanics,* Elsevier, London, 1991.